agreement with the size of the estimated pseudofield (45 nm). The density-of-states peaks observed as weakly negative sloping lines in the gate maps (Fig. 3A) may be caused by localization in a spatially varying pseudofield (*6*, *7*, *10*), although a detailed model is currently not available. The variations in positive-slope bands (Fig. 3, B to D) are probably caused by minor deformations of the overall membrane shape affecting the size of the QD.

References and Notes

1. K. S. Novoselov *et al.*, *Proc. Natl. Acad. Sci. U.S.A.* **102**, 10451 (2005).
2. K. I. Bolotin *et al.*, *Solid State Commun.* **146**, 351 (2008).
3. M. M. Fogler, F. Guinea, M. I. Katsnelson, *Phys. Rev. Lett.* **101**, 226804 (2008).
4. F. Guinea, M. I. Katsnelson, A. K. Geim, *Nat. Phys.* **6**, 30 (2010).
5. N. Levy *et al.*, *Science* **329**, 544 (2010).
6. K.-J. Kim, Y. M. Blanter, K.-H. Ahn, *Phys. Rev. B* **84**, 081401 (2011).
7. G. M. M. Wakker, R. P. Tiwari, M. Blaauboer, *Phys. Rev. B* **84**, 195427 (2011).
8. F. Guinea, B. Horovitz, P. Le Doussal, *Phys. Rev. B* **77**, 205421 (2008).
9. F. Guinea, A. K. Geim, M. I. Katsnelson, K. S. Novoselov, *Phys. Rev. B* **81**, 035408 (2010).
10. T. O. Wehling, A. V. Balatsky, A. M. Tsvelik, M. I. Katsnelson, A. I. Lichtenstein, *Europhys. Lett.* **84**, 17003 (2008).
11. M. Gibertini, A. Tomadin, M. Polini, *Phys. Rev. B* **81**, 125437 (2010).
12. S. Jung *et al.*, *Nat. Phys.* **7**, 245 (2011).
13. A. Luican, G. Li, E. Y. Andrei, *Phys. Rev. B* **83**, 041405 (2011).
14. J. A. Stroscio, E. W. Hudson, S. R. Blankenship, R. J. Celotta, A. P. Fein, *Proc. SPIE* **4608**, 112 (2002).
15. G. M. Rutter *et al.*, *Nat. Phys.* **7**, 649 (2011).
16. D. L. Miller *et al.*, *Science* **324**, 924 (2009).
17. G. Li, A. Luican, E. Y. Andrei, *Phys. Rev. Lett.* **102**, 176804 (2009).
18. Additional supplementary text and data are available on *Science* Online.
19. B. J. LeRoy, J. Kong, V. K. Pahilwani, C. Dekker, S. G. Lemay, *Phys. Rev. B* **72**, 075413 (2005).
20. L. P. Kouwenhoven, D. G. Austing, S. Tarucha, *Rep. Prog. Phys.* **64**, 701 (2001).
21. We determined the 1 SD error estimates in the QD sizes by combining the 1 SD in the addition energy variation for the first and last set of energies in Fig. 3G, together with the 1 SD uncertainties in the measured slopes of the charging lines in the gate maps.
22. M. I. Katsnelson, K. S. Novoselov, A. K. Geim, *Nat. Phys.* **2**, 620 (2006).
23. J. Güttinger *et al.*, *Phys. Rev. Lett.* **103**, 046810 (2009).

Acknowledgments: We thank M. Stiles and S. Adam for valuable discussions and S. Blankenship and A. Band for technical assistance. The U.S. National Science Foundation is gratefully acknowledged via grants CMMI-1069076 and CMMI-1129826 (T.L. and S.Z.) and grant CMMI-0841840 (C.A.W. and S.D.S.).

Supplementary Materials

www.sciencemag.org/cgi/content/full/336/6088/1557/DC1
Supplementary Text
Figs. S1 to S13
References (*24*–*26*)

9 February 2012; accepted 30 April 2012
10.1126/science.1220335

Electrical Wind Force–Driven and Dislocation-Templated Amorphization in Phase-Change Nanowires

Sung-Wook Nam,[1]* Hee-Suk Chung,[1]* Yu Chieh Lo,[1,2] Liang Qi,[1,2] Ju Li,[1,2] Ye Lu,[3] A.T. Charlie Johnson,[1,3] Yeonwoong Jung,[1] Pavan Nukala,[1] Ritesh Agarwal[1]†

Phase-change materials undergo rapid and reversible crystalline-to-amorphous structural transformation and are being used for nonvolatile memory devices. However, the transformation mechanism remains poorly understood. We have studied the effect of electrical pulses on the crystalline-to-amorphous phase change in a single-crystalline $Ge_2Sb_2Te_5$ (GST) nanowire memory device by in situ transmission electron microscopy. We show that electrical pulses produce dislocations in crystalline GST, which become mobile and glide in the direction of hole-carrier motion. The continuous increase in the density of dislocations moving unidirectionally in the material leads to dislocation jamming, which eventually induces the crystalline-to-amorphous phase change with a sharp interface spanning the entire nanowire cross section. The dislocation-templated amorphization explains the large on/off resistance ratio of the device.

Chalcogenide-based phase-change memory (PCM) materials have been widely used for optical data storage and are now finding applications in electronic memory devices (*1*, *2*). In a nonvolatile PCM device, the difference in optical reflectivity or electrical resistance between amorphous and crystalline phases is used to store information. Memory switching is performed by applying optical (or electrical) pulses: short pulses with large amplitude to amorphize the material and long pulses with low amplitude for the crystallization process. It has been generally assumed that the large amplitude of the pulse melts the material, and its short duration locks the atoms in their disordered positions owing to rapid quenching. The understanding of the effects of electric field on the crystalline-to-amorphous phase transition in PCM is critical for designing low-power nonvolatile memory devices. Therefore, it is desirable to visualize and characterize the critical events that lead to the phase-change process while the device is under operation, which can uncover phenomena that cannot be gleaned from ex situ measurements (*3*). However, it is challenging to resolve the amorphization phenomena with high spatial and/or temporal resolution in confined structures such as in conventional thin-film devices with a sandwich geometry (*4*). Very recently, based on time-resolved photo-excitation measurements of PCM materials (*5*, *6*), it has been argued that the material did not amorphize via the liquid-state pathway, but by a solid-state, lattice-distortion–triggered process. Consequently, visualization of the structural evolution of the PCM device under electrical biasing by correlating it to the electrical-resistance variation would be helpful. A single-crystalline device can serve as an ideal platform to study the relationship between microstructural evolution and electrical resistance variation, so as to avoid the effects of preexisting grain boundaries on carrier transport and structural dynamics. In conventional PCM devices, polycrystalline thin films with relatively small grain sizes (10 to 20 nm) preclude the visualization of switching behavior originating from single grains. By using the single-crystalline, lateral, and open geometry of the $Ge_2Sb_2Te_5$ (GST) nanowire structure, we visualized the amorphization behavior and found it to be critically associated with the nucleation and dynamics of dislocations.

We assembled GST nanowire memory devices across 2-μm-wide trenches fabricated on a thin silicon-nitride membrane (Fig. 1A) to enable real-time visualization of nanoscale structural changes with high spatial resolution under the influence of applied electrical voltage pulses inside a transmission electron microscope (TEM) (figs. S1 to S4) (*7*). Single-crystalline GST nanowires with hexagonal crystal structure grown along the $[10\bar{1}0]$ axis were synthesized through the vapor-liquid-solid method (fig. S1) (*8*). For device operation, voltage pulses with duration of a few hundred nanoseconds were applied, and between each pulse, the resistance was measured at a DC bias of 0.2 V (Fig. 1B). We note that all the reported electrical resistances in this paper are not the dynamic resistances during electrical pulsing, but the stationary resistance values of the devices measured long after the pulsing process so that the heat generated during the pulsing was dissipated and the devices reached room temperature. The resistance (after each 300-ns pulse with increasing voltage amplitude)

[1]Department of Materials Science and Engineering, University of Pennsylvania, Philadelphia, PA 19104, USA. [2]Department of Nuclear Science and Engineering and Department of Materials Science and Engineering, Massachusetts Institute of Technology, Cambridge, MA 02139, USA. [3]Department of Physics and Astronomy, University of Pennsylvania, Philadelphia, PA 19104, USA.

*These authors contributed equally to this work.
†To whom correspondence should be addressed. E-mail: riteshag@seas.upenn.edu

of a 280-nm-thick GST nanowire device as a function of the pulse amplitude (Fig. 1C, blue squares) decreases slightly above 3.3 V, just before amorphization electrical switching was observed. The resistance dip, however, was very small as compared with the more than two orders of magnitude increase in the electrical resistance associated with amorphization switching. There are some critical observations related to the resistance dip: (i) The decrease in the electrical resistance reflects a permanent structural change in the device while still in the crystalline state; and (ii) the critical voltage at which the resistance starts to decrease is a function of the nanowire thickness and pulse width (Fig. 1C and fig. S5). The voltage at which the resistance dip initiates decreased with increasing pulse width, and thicker wires required higher voltages and longer pulses (Fig. 1C, inset).

To correlate the onset of the resistance dip and amorphization with structural evolution, we show snapshots of the dark-field (DF) TEM movie (movie S1) and the corresponding electrical resistances of a nanowire device in Fig. 2. The resistance dip before amorphization was a general feature of all nanowire devices measured either inside or outside the TEM. For a 230-nm nanowire device, no structural changes in the DF TEM images were identified until ~5 V pulses (800 ns), but concomitant with the onset of the resistance dip, the uniform contrast of the single-crystalline device started to change dynamically, with extended line-shaped defects (Fig. 2B) and other strain-related contrasts. For voltages below the resistance dip (<5.8 V), the contrast continued to change upon each applied pulse, but no directional motion was observed. High-resolution TEM characterization of the line defects reveals the presence of dislocations (fig. S6) with a Burgers vector of $\frac{1}{2}\langle 11\bar{2}0\rangle$. Considering the hexagonal-crystalline structure of GST grown along the $[10\bar{1}0]$ axis, the line-shape structure represents the projection image of the dislocation loop that lies on the $(10\bar{1}0)$ prismatic plane, as illustrated in Fig. 1A.

Notably, upon further increasing the voltage pulse amplitude (800 ns duration), the resistance dip was directly associated with the line defects becoming mobile and propagating along the direction of hole-carrier motion (Fig. 2, C to F). This observation suggests the influence of the carrier wind force to break the symmetry of the nanowire for dislocation motion, thereby inducing a polarity-dependent behavior (*9*–*11*). The resistance continued to drop with the increase in the pulse amplitude, accompanied with the motion of dislocations from the positive to the negative electrode. In particular, dynamic contrast changes were observed moving unidirectionally in the device. Upon approaching the bottom of the resistance dip, it was observed that the dislocations stopped moving (jamming), followed by the formation of highly accumulated and entangled dislocations at the jammed location (Fig. 2, G and H, and movie S1). Finally, amorphization switching was observed, accompanied by an increase in the electrical resistance by approximately two orders of magnitude. A clear bright line was identified as the amorphous phase (red arrow, Fig. 2I), which was further characterized by electron diffraction studies (fig. S7). TEM image of the free-standing region of the nanowire (over the trench) in Fig. 2J shows a trail of dislocation cloud right behind the amorphized region. In addition, a few other dislocation cloud trails were identified along the nanowire but without any amorphous marks, which indicates that they got jammed by random perturbation in the nanowire structure, with one among them eventually undergoing amorphization. These observations show that the entangled dislocations

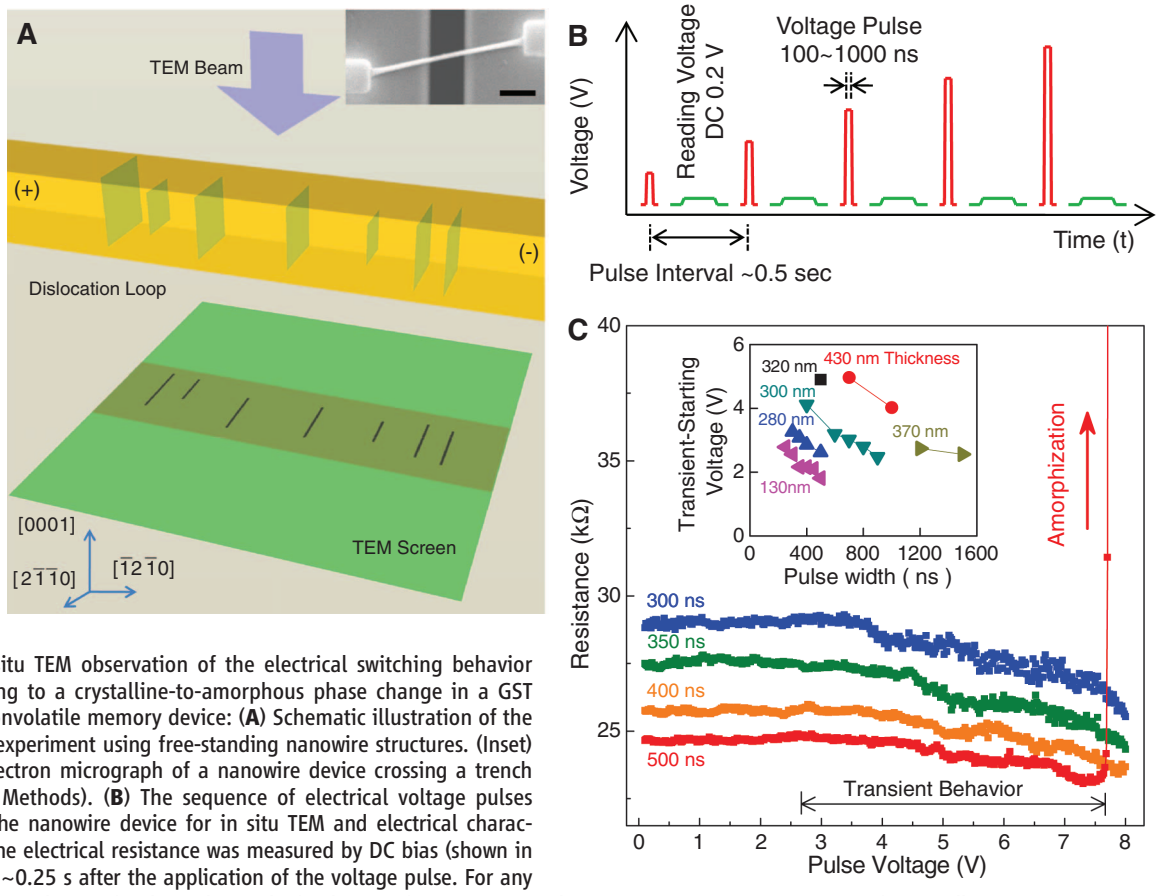

Fig. 1. In situ TEM observation of the electrical switching behavior corresponding to a crystalline-to-amorphous phase change in a GST nanowire nonvolatile memory device: (**A**) Schematic illustration of the in situ TEM experiment using free-standing nanowire structures. (Inset) Scanning electron micrograph of a nanowire device crossing a trench region (see Methods). (**B**) The sequence of electrical voltage pulses applied to the nanowire device for in situ TEM and electrical characterization. The electrical resistance was measured by DC bias (shown in green) after ~0.25 s after the application of the voltage pulse. For any pulse sequence, the amplitude of the applied voltage pulse was increased with a 0.5-s interval between any two pulses while their widths were kept constant. (**C**) Plots of electrical resistance of the nanowire device versus applied voltage pulse amplitude obtained for different pulse width sequences, starting from a single-crystalline state. Resistance dip was observed before amorphization switching. (Inset) A plot of nanowire size versus the voltage at which the resistance dip is initiated as a function applied pulse widths.

caused by dislocation generation and jamming are precursors for the amorphization switching of the device.

To confirm that the electrical polarity determines the direction of propagation of dislocations by the carrier wind force, we performed a "reverse-bias" experiment with the opposite polarity applied on the same device (Fig. 2, K to T, and movie S2). The device was first switched back to the crystalline state, followed by the continuous application of electrical pulses with the opposite polarity in the same sequence as described above. Upon applying 500-ns-width pulses, the resistance dip was observed, during which the jammed dislocation cloud from the previous measurement was relieved by moving in the opposite direction. We then stopped pulsing at 5 V, and then applied 800-ns pulses starting from 0 V. The device resistance started from the resistance at which we stopped the 500-ns pulses (Fig. 2K), which then began to dip again from ~2 V (longer pulses lead to onset of resistance dip at lower voltages). Dynamic contrast changes were observed to move in the opposite direction, which again corresponds to the direction of the hole carriers (movie S2). Eventually, amorphization switching occurred at ~5.2 V (Fig. 2, P to S), with the dislocation cloud appearing behind the amorphous mark, consistent with the forward-bias experiments (Fig. 2T). The reverse-bias pulsing experiment clearly indicates that the mobile dislocations are transported in the direction of the applied bias, which is the direction of the motion of hole carriers in the device, suggesting a critical role of dislocation nucleation, motion, and jamming in creating the amorphous phase in the PCM device.

To better visualize the amorphization switching process, we sculpted a notch structure in the nanowire suspended over the trench to localize the phase-change region at the notch (Fig. 3) (*3*). In bright-field (BF) TEM image, the as-fabricated nanowire appeared uniformly dark owing to its single crystallinity (Fig. 3A). During electrical pulsing (movie S3), a change in the

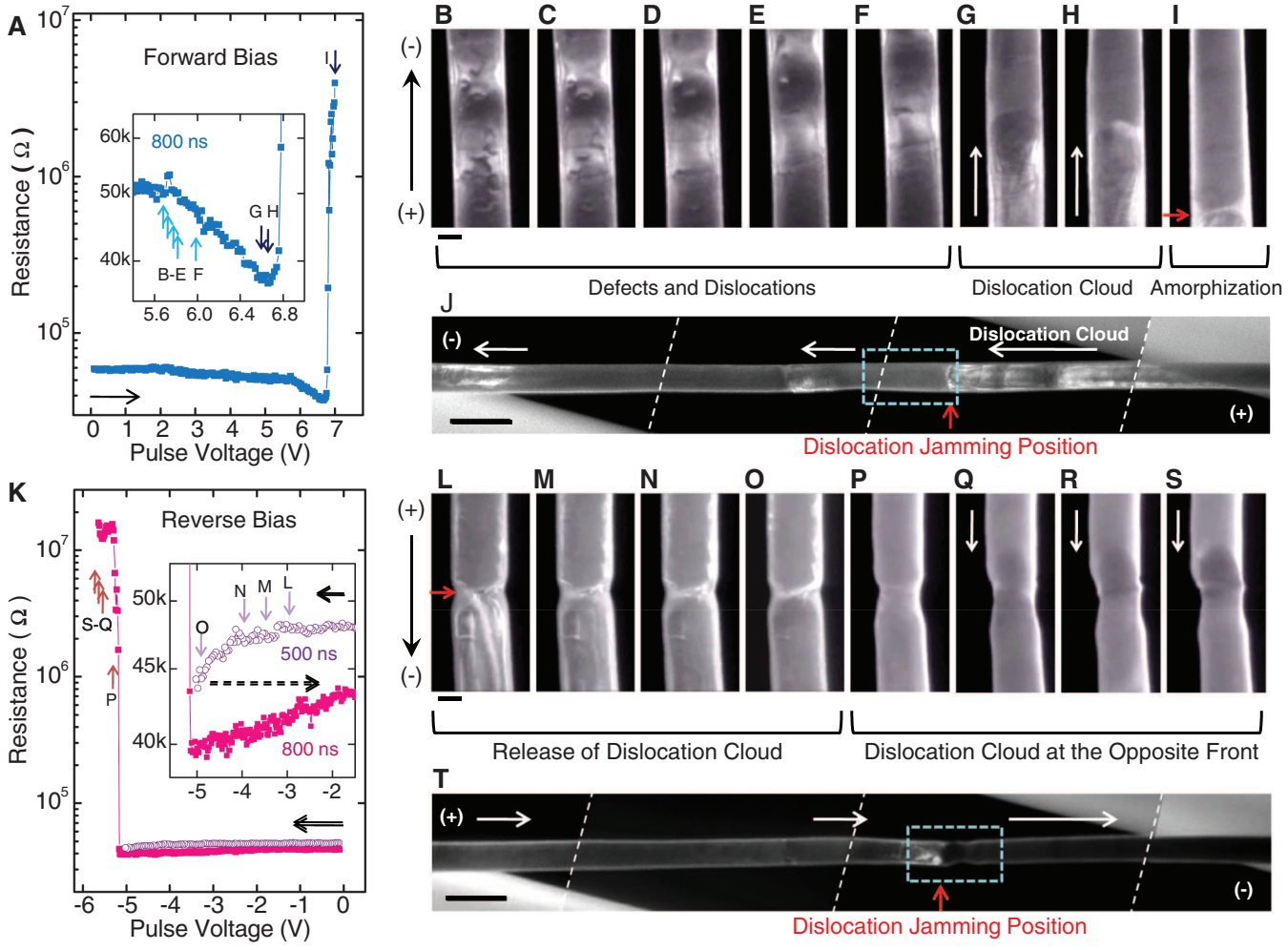

Fig. 2. Electric wind force–driven mobile dislocations and amorphization switching via in situ TEM measurements: (**A** to **J**) "Forward-bias"; (**K** to **T**) "reverse-bias," i.e., opposite polarity from the same region of the device. (A) Plot of stationary electrical resistance of the nanowire device versus voltage pulse amplitude for the forward-bias direction. The electrical resistance states are correlated with the TEM images of the device, as indicated by arrows. (B to I) Snapshots of DF TEM images (from movie S1) during electrical switching: At the early stage, individual dislocations were identified in (B) to (E), which started to propagate along the hole-carrier motion direction (F to I). The white arrows indicate the unidirectional motion of the TEM image contrast. At the bottom of the electrical resistance dip, a dislocation cloud was observed in (G) and (H). Following the resistance dip regime, amorphization occurred at the dislocation jamming region [red arrow in (I)]. (J) Larger-area DF TEM image of the free-standing GST nanowire device after amorphization, showing a dislocation trail behind the amorphized region. The blue rectangular area was recorded in the TEM movie (movie S1). (K) Plot of electrical resistance versus voltage pulse amplitude for the reverse-bias case. (L to S) From movie S2; the dislocation cloud behind the jamming region was first relieved (L to O), and subsequently another dislocation cloud was developed on the opposite front of the jamming transition region (P to S). (T) Larger-area DF TEM image of the nanowire after the reverse-polarity–biased amorphization switching, again showing a dislocation trail behind the amorphized region, but in the opposite direction as compared with (J). Scale bar: (B to I) and (L to S), 100 nm; (J and T), 500 nm. The dashed lines in (J) and (T) denote the regions where the images were combined.

image contrast was observed while the device was still in the crystalline state, with the notch region developing a dark line contrast (Fig. 3B), followed by a contrast variation moving from the positive- to the negative-electrode side (Fig. 3C). The image contrast variation along the nanowire was again correlated with the resistance dip, consistent with our previous observations for the non-notched devices. Finally, upon amorphization switching, the dark line in the middle of the notch was abruptly changed into a bright amorphous band (Fig. 3D). Microstructure analysis (BF TEM images) both before and after the switching (fig. S8) shows that a highly strained structure developed in the notch region before amorphization. In particular, the amorphous mark appeared in this region of strain, which suggests the role of strain in the amorphization process. The origin of the strained structure and the differential contrast was further studied by DF TEM analysis (Fig. 3E). DF TEM revealed the presence of a high density of dislocations, predominantly at the positive-electrode side of the notch (Fig. 3E). Even though the notch structure was intended to localize joule heating by enhancing the current density, our in situ observation additionally suggests that the notch was also more likely to behave as a geometrical necking region where mobile dislocations were jammed and accumulated by the electrical wind force that did not pass through the constriction easily (see also fig. S9 for results from another device).

In contrast to thin-film polycrystalline GST, which consists of small grains (10 to 20 nm), the single-crystalline nanowire structure rules out the effect of preexisting grain boundaries for both structural evolution and resistance dip. Our observations show that the dislocations are continuously nucleated along the single-crystalline GST nanowire, which become mobile above a certain applied voltage that is correlated to the resistance dip. The voltage pulses play a critical role by inducing heat shocks along the single-crystalline nanowire, which create dislocations by vacancy condensation (*12*). The rising edge of the pulse produces lattice vacancies in the material caused by heating, with the nanowire surface/interface serving as the lattice vacancy source, whereas during rapid cooling, atomic vacancies are condensed into dislocation loops by nonconservative dislocation climb (*12*, *13*) (fig. S10). This mass-action dislocation generation path is different from purely displacive shear nucleation driven by an external mechanical stress (*14*–*18*). Because our nanowire is a free-standing structure where the thermal-expansion stress is relieved from its surface (*19*) and by buckling, the dislocation formation is attributed more to vacancy supersaturation (osmotic forces) than to mechanical stress. After formation, these dislocations feel the directional electrical wind force, but display a threshold behavior in mobility: that is, as a whole, they only start to move when the electrical wind force exceeds a critical value. When the dislocations become mobile, they consume more vacancies along the way by combined climb and glide actions, which decrease the carrier scattering probability, thereby decreasing the electrical resistance of the device (Fig. 1C) (*13*). (Dislocation dynamics are illustrated in figures S11 to S14.) Similar electrical resistance drops have been observed during rapid annealing of metals, attributed to Frank and prismatic dislocation loop nucleation and growth driven by vacancy condensation (*13*). Therefore, we believe that an electrical current pulse has two physical effects, one directional and the other nondirectional. The nondirectional thermal heating and quenching produce the dislocations, whereas the directional wind force moves the dislocations in the drift direction of the majority charge carrier (holes in the case of GST), leading to polarity dependence. Yang *et al*. (*10*) have reported that hole-carrier wind force in GST induces a mass transport by electromigration at high current densities, which partly corroborates our observation of polarity-dependent dislocation motion.

One question that arises naturally is, what specific properties of GST lead to the observation of dislocation nucleation and transport, which is quite different from those in other covalently bonded materials such as silicon? To understand dislocation transport in crystalline hexagonal GST, we performed ab initio density functional theory (DFT) calculations to characterize slip systems of a prismatic dislocation loop. The DFT calculations for basal $(0001)[11\bar{2}0]$ and prismatic $(1\bar{1}00)[11\bar{2}0]$ slips exhibit unstable generalized-stacking-fault (GSF, γ) energies of 10.1 and 172.8 mJ/m^2, respectively (Fig. 4A and fig. S15). $\gamma_{\text{unstable}}^{(0001)[11\bar{2}0]}$ is extremely small [similar to basal slip in graphite (*20*)]; in GST-layered structures with

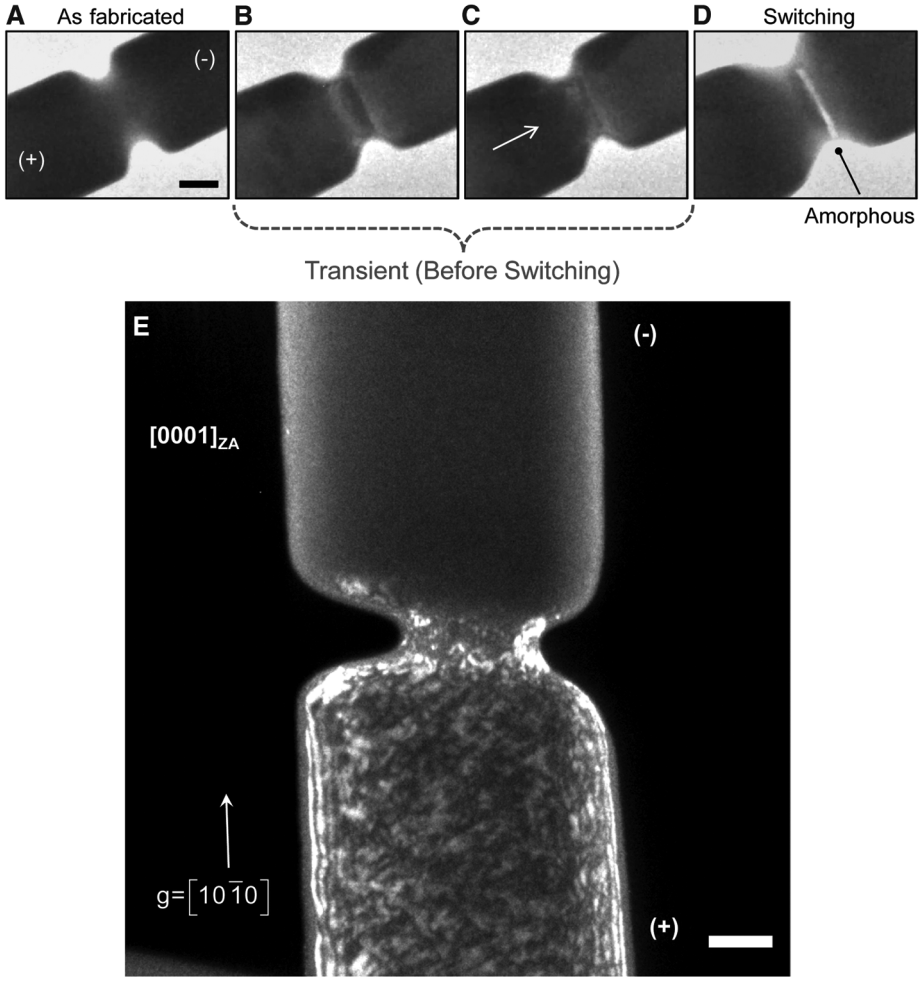

Fig. 3. Transient behavior (region of resistance dip) followed by amorphization switching for a nanowire device with a notch (constriction). (**A** to **D**) Snapshots from BF TEM movie (movie S3): As-fabricated nanowire device shows a uniform, dark contrast along the nanowire in (A). As the electrical pulses were applied, the variation in TEM image contrast was identified at the moment of the initiation of the resistance dip. Darker line in the middle of the notch in (B) and (C) shows a region of highly concentrated strain, which was changed into bright contrast upon amorphization (D). (**E**) DF TEM image of the single-crystalline nanowire close to the bottom of the transient resistance dip: A dislocation cloud was located mostly at the (+) electrode region in (E). Scale bars (A and E), 100 nm.

a stacking sequence -Sb-Te-Ge-Te-Te-Ge-Te-Sb-Te- (also occurs in cubic GST) (*21*), weak Te-Te bonding on the basal plane is the most likely to slip because of its long bond length and weak bonding energy (*22*). $\gamma_{unstable}^{(1\bar{1}00)[11\bar{2}0]}$ is quite small also, comparable to that for partial dislocation slip in Cu (169 mJ/m^2) (*23*), and much smaller than those for slips in Si (>1500 mJ/m^2) (*24*); thus, motion of prismatic dislocation loops driven by the electrical wind force is feasible in GST (for crystallographic details on glide of prismatic loops, refer to figs. S11 to S14).

We summarize the dislocation generation and dynamics leading to amorphization switching in Fig. 4B. Both heat (nondirectional) and carrier wind force (directional) effects are consequences of the applied voltage pulses. Just before the initiation of the resistance dip, the heat-shock process by the electrical pulses leads to generation of vacancies followed by their rapid condensation to generate dislocations, analogous to generation of Frank-partial and prismatic dislocations in face-centered cubic metals by vacancy condensation (*25*). From our observation, it is likely that most of the dislocations are generated at the positive-bias metal electrode in contact with the nanowire (owing to material incompatibility and larger potential drop), but some of them can also be generated along the nanowire. As the amplitude of voltage pulses increases, the carrier wind force makes the dislocations mobile, gliding as prismatic dislocation loops. These dislocation loops grow in size as they move, encounter, and annihilate more vacancies, acting as "garbage collectors," which decrease the total disorder in the crystal, but also transport some disorder (in the form of dislocation cores) downstream in a one-dimensional (1D) traffic flow along the nanowire.

One-dimensional traffic flows are inherently fragile and prone to instabilities, because of interactions between the mobile agents that lead to density-dependent mobility (*26*). For instance, analytical models of automobile traffic on a highway predict sharp, catastrophic jamming when the automobile density exceeds a certain fraction of the maximum packing density (*27*). Owing to the mutual tangling that lowers their 1D mobility, the mobile dislocations moving in the direction of the hole drift can jam at some location. The dislocations then accumulate at the jammed region of the nanowire, which creates a high degree of disorder locally in the crystalline material, leading eventually to amorphization switching (*28*–*31*). Therefore, paradoxically, the mobile extended defects, which decrease the crystalline disorder elsewhere, can also greatly concentrate the disorder in a local region, when the jamming transition occurs. For nanowires without a notch, the dislocation jamming can occur anywhere when a critical dislocation density is reached in the system.

Our observations show that amorphization in PCM devices is templated by dislocation transport and jamming in the crystal. If the devices were amorphized by conventional melt-quench process, then one would have expected initiation of melting from the nanowire surface that should have spread, eventually leading to an amorphous shell around a crystalline core. Such a mechanism would have led to poor on/off resistance ratios because of resistors in parallel. In contrast, we have always observed the amorphous phase form in series with the crystalline phase (*3*), with the amorphous volume occupying just a tiny fraction of the total device volume, yet achieving good device performance with large on/off resistance ratios. Furthermore, in all the measured devices, the amorphous mark always appeared in front of the jammed dislocation cloud spanning the entire cross section of the nanowire and with very sharp vertical interfaces, with no amorphous phase seen anywhere else. It is thus evident that the dislocation jam with vertical boundaries provides a microstructural template for amorphization to occur in a vertical section, which is different from conventional understanding of melting that is templated by free surfaces. Solid-state amorphization is known to occur in silicon (*29*) and metallic (*31*) crystals by mechanical ball milling that injects a high density of dislocations into the material, where melting is not possible at room temperature. We cannot completely rule out the possibility of transient melting in the dislocated region, because dislocations do increase the local resistance and heat generation. The physics of such atomic disordering around dislocation cores—i.e., premelting (*32*)—even if it occurs, would be quite different from normal melting, because the degree of atomic disordering around dislocation cores can only rise gradually with temperature, unlike a sharp first-order thermodynamic transition in a conventional bulk melting process. In any case, our main result, which is dislocation-templated amorphization of narrow cross section with a sharp interface, is microstructural—independent of the detailed chemical physics of atomic disordering—and consistent with the observed device performance (large on/off ratio). Our results, based on direct observation by in situ TEM analysis, are consistent with several recent reports (*5*, *6*, *33*) that also have suggested non- (conventional) melting–based amorphization process in GST material.

The observation of the voltage pulse–induced dislocation nucleation, wind force–assisted dislocation glide and jamming, and subsequent dislocation-templated amorphization shed light on previously unexplored properties of these fascinating materials, relating microstructural evolution to device properties. A similar mechanism could operate in polycrystalline thin-film devices as the grain boundaries can be considered as networks of dislocations and also act as dislocation sources and sinks. Furthermore, direct visualization of various processes occurring in PCM devices under electrical bias would be promising to understand their unusual fast switching behavior and will also be applicable to other functional materials and devices.

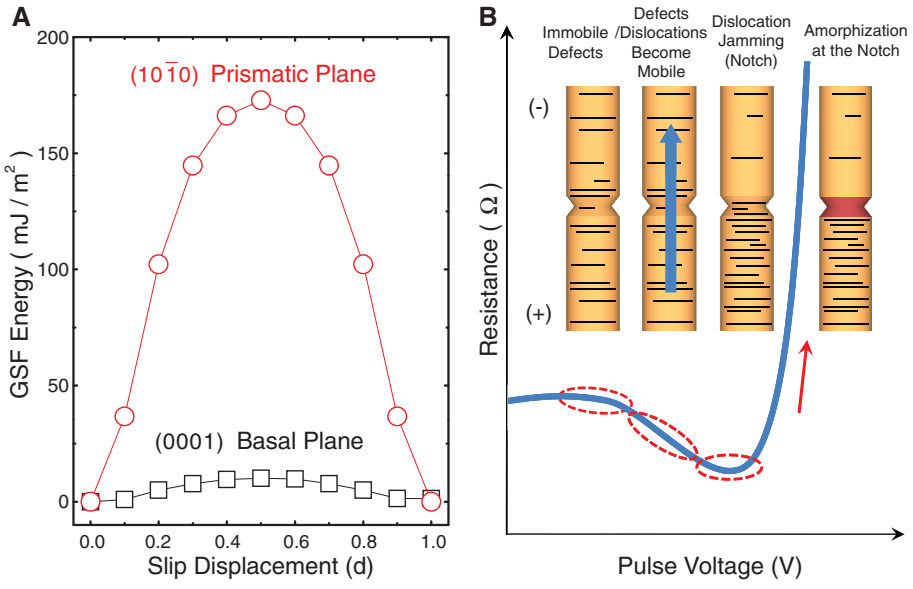

Fig. 4. (**A**) DFT calculation of generalized stacking fault (GSF) energy for both basal (0001) and prismatic (10$\bar{1}$0) planes in hexagonal $Ge_2Sb_2Te_5$. (**B**) Our model of dislocation nucleation, transport, and jamming by electrical pulses: At the initiation of the dip of electrical resistance, the electrical pulses induce heat shocks to nucleate dislocations from atomic vacancies. As the pulse voltage amplitude increases, the dislocations become mobile and move along the direction of holes owing to the carrier wind force. Eventually, because of the increase in dislocation density, there is a jamming transition (e.g., in the notch region or elsewhere for regular wires), where the dislocations pile up, followed by amorphous switching in the same region. On the other side of the notch, the dislocations move away from the observed region in TEM owing to wind force.

References and Notes

1. M. Wuttig, N. Yamada, *Nat. Mater.* **6**, 824 (2007).
2. S. Raoux, *Annu. Rev. Mater. Res.* **39**, 25 (2009).
3. Y. Jung, S. W. Nam, R. Agarwal, *Nano Lett.* **11**, 1364 (2011).
4. B. J. Kooi, W. M. G. Groot, J. T. M. De Hosson, *J. Appl. Phys.* **95**, 924 (2004).
5. P. Fons *et al.*, *Phys. Rev. B* **82**, 041203(R) (2010).
6. A. V. Kolobov, M. Krbal, P. Fons, J. Tominaga, T. Uruga, *Nat. Chem.* **3**, 311 (2011).
7. D. R. Strachan *et al.*, *Phys. Rev. Lett.* **100**, 056805 (2008).
8. S. H. Lee, Y. Jung, R. Agarwal, *Nat. Nanotechnol.* **2**, 626 (2007).
9. S. W. Nam *et al.*, *Electrochem. Solid-State Lett.* **12**, H155 (2009).
10. T. Y. Yang, I. M. Park, B. J. Kim, Y. C. Joo, *Appl. Phys. Lett.* **95**, 032104 (2009).
11. M. H. Lee *et al.*, *IEEE International Electron Devices Meeting (IEDM)*, 28.6.1. (2010).
12. G. Schoeck, W. A. Tiller, *Philos. Mag.* **5**, 43 (1960).
13. H. Kimura, R. Maddin, D. Kuhlmannwilsdorf, *Acta Metall.* **7**, 145 (1959).
14. H. Zheng *et al.*, *Nat. Commun.* **1**, 144 (2010).
15. Z. W. Shan, R. K. Mishra, S. A. Syed Asif, O. L. Warren, A. M. Minor, *Nat. Mater.* **7**, 115 (2008).
16. S. H. Oh, M. Legros, D. Kiener, G. Dehm, *Nat. Mater.* **8**, 95 (2009).
17. Q. Yu *et al.*, *Nature* **463**, 335 (2010).
18. T. Zhu, J. Li, A. Samanta, A. Leach, K. Gall, *Phys. Rev. Lett.* **100**, 025502 (2008).
19. M. Mitra, Y. Jung, D. S. Gianola, R. Agarwal, *Appl. Phys. Lett.* **96**, 222111 (2010).
20. R. H. Telling, M. I. Heggie, *Philos. Mag. Lett.* **83**, 411 (2003).
21. A. V. Kolobov *et al.*, *Nat. Mater.* **3**, 703 (2004).
22. Z. M. Sun, J. Zhou, R. Ahuja, *Phys. Rev. Lett.* **96**, 055507 (2006).
23. S. Ogata, J. Li, S. Yip, *Phys. Rev. B* **71**, 224102 (2005).
24. E. Kaxiras, M. S. Duesbery, *Phys. Rev. Lett.* **70**, 3752 (1993).
25. D. Hull, D. J. Bacon, *Introduction to Dislocations* (Butterworth-Heinemann, Oxford, ed. 4, 2001).
26. K. Nagel, *Phys. Rev. E Stat. Phys. Plasmas Fluids Relat. Interdiscip. Topics* **53**, 4655 (1996).
27. D. Helbing, *Rev. Mod. Phys.* **73**, 1067 (2001).
28. D. Wolf, P. R. Okamoto, S. Yip, J. F. Lutsko, M. Kluge, *J. Mater. Res.* **5**, 286 (1990).
29. J. Y. Huang, H. Yasuda, H. Mori, *Philos. Mag. Lett.* **79**, 305 (1999).
30. J. Y. Huang *et al.*, *Science* **330**, 1515 (2010).
31. J. Y. Huang, Y. T. Zhu, X. Z. Liao, R. Z. Valiev, *Philos. Mag. Lett.* **84**, 183 (2004).
32. Y. Mishin, M. Asta, J. Li, *Acta Mater.* **58**, 1117 (2010).
33. A. V. Kolobov *et al.*, *Phys. Rev. Lett.* **97**, 035701 (2006).

Acknowledgments: This work was supported by the Office of Naval Research (grant N000140910116), Materials Structures and Devices Center at the Massachusetts Institute of Technology, NSF (DMR-0706381 and DMR-1002164), and Penn-Materials Research Science and Engineering Center (DMR05-20020 and DMR11-20901). Y.C.L., L.Q., and J.L. acknowledge the support of NSF DMR-1008104 and DMR-1120901, and Air Force Office of Scientific Research FA9550-08-1-0325. Y.L. and A.T.C.J. acknowledge the support of the Nano/Bio Interface Center through NSF Nanoscale Science and Engineering Center DMR08-32802. Electron microscopy experiments were performed at the Penn Regional Nanotechnology Facility at the University of Pennsylvania. S.-W.N. thanks D. Strachan for useful discussions on in situ TEM experiments. The data described in the paper are archived by the Agarwal group at the University of Pennsylvania.

Supplementary Materials

www.sciencemag.org/cgi/content/full/336/6088/1561/DC1
Materials and Methods
Figs. S1 to S15
References
Movies S1 to S3

6 February 2012; accepted 18 May 2012
10.1126/science.1220119

Breaking the Speed Limits of Phase-Change Memory

D. Loke,[1,2,3]* T. H. Lee,[2]* W. J. Wang,[1] L. P. Shi,[1]† R. Zhao,[1] Y. C. Yeo,[4] T. C. Chong,[5] S. R. Elliott[2]†

Phase-change random-access memory (PCRAM) is one of the leading candidates for next-generation data-storage devices, but the trade-off between crystallization (writing) speed and amorphous-phase stability (data retention) presents a key challenge. We control the crystallization kinetics of a phase-change material by applying a constant low voltage via prestructural ordering (incubation) effects. A crystallization speed of 500 picoseconds was achieved, as well as high-speed reversible switching using 500-picosecond pulses. Ab initio molecular dynamics simulations reveal the phase-change kinetics in PCRAM devices and the structural origin of the incubation-assisted increase in crystallization speed. This paves the way for achieving a broadly applicable memory device, capable of nonvolatile operations beyond gigahertz data-transfer rates.

Phase-change random-access memory (PCRAM) represents one of the best candidates for a so-called "universal memory" due to its nonvolatile nature, high scalability, low power consumption, high read/write speeds, and long read/write endurance (*1*–*4*). PCRAM operations, based on the reversible switching of phase-change (PC) materials between amorphous and crystalline states (*5*, *6*), are generally fast: on the order of nanosecond time scales (*7*–*9*). However, the crystallization speed is much slower than the amorphization speed, which limits the overall writing speed of PCRAMs. Despite efforts (*10*–*16*) to increase the crystallization speed, it has been difficult to achieve a speed faster than 1 ns. A difficulty arises from the contradictory nature of increasing the crystallization speed while extending the stability of PC materials for long-term data retention (*17*). This has restricted the selection of PC materials in the commercial development of PCRAMs, typically emphasizing high stability at the expense of crystallization speeds.

According to classical nucleation theory, the nucleation of small crystallites and their subsequent growth are the two main distinct processes in crystallization (*18*–*20*). The nucleation rate is faster at lower temperatures, followed by rapid growth at higher temperatures (*21*). We show that by stimulating and altering these processes, we are able to control the speed of crystallization by electrical means. Our approach is based on the idea of providing a weak electric field to induce thermal prestructural ordering (incubation of ordered clusters in the amorphous matrix) via Joule heating, which enables faster nucleation and growth upon a subsequent stronger electrical pulse, while maintaining the high stability of the amorphous phase by controlling the cluster-size distribution (Fig. 1). This thermal-incubation model is very different from the model of Karpov *et al.* (*22*), which assumes a direct electric-field–induced modification of the crystal-nucleation barriers in $Ge_2Sb_2Te_5$ (GST).

We experimentally fabricated porelike structured PCRAM cells (with GST as the PC material) and used these cells to study the incubation effects on the crystallization speeds (Fig. 1D) (*23*). To study the ultrafast switching effects, a weak electric field (equivalent to ~0.3 V), for tailoring the crystallization kinetics (hereafter referred to as the incubation field), was employed to achieve optimal switching properties without activating spontaneous crystallization (fig. S2). We employed subsequent electrical pulses (varying in length from several hundred picoseconds to several tens of nanoseconds) to switch the cells, and we used the full width at half maximum (FWHM) values of the pulses to characterize the switching speeds of the cells (fig. S3). The duration of a pulse experienced in the cell was confirmed to be the same as that measured before the pulse enters the cell (fig. S4).

We found that the incubation field, even with the small amount of thermal energy it delivers, can substantially promote the nucleation and growth of PC materials. Nucleation and growth times can be characterized by the minimum electrical pulse width needed to switch the cell from the amorphous state to the crystalline state (*24*), also known as the "set" process. When the incubation field is applied to a cell (Fig. 2A), much faster nucleation and growth are observed, as manifested by the substantial decrease in pulse width (by ~5 ns). For the fastest nucleation and growth, we found the shortest pulse to be 500 ps. This is approximately one order of magnitude

[1]Data Storage Institute, Agency for Science, Technology and Research (A*STAR), 5 Engineering Drive 1, Singapore 117608. [2]Department of Chemistry, University of Cambridge, Lensfield Road, Cambridge CB2 1EW, UK. [3]National University of Singapore (NUS) Graduate School for Integrative Sciences and Engineering, 28 Medical Drive, Singapore 117456. [4]Department of Electrical and Computer Engineering, National University of Singapore, 4 Engineering Drive 3, Singapore 117576. [5]Singapore University of Technology and Design, 20 Dover Drive, Singapore 138682.

*These authors contributed equally to this work.
†To whom correspondence should be addressed. E-mail: shi_luping@dsi.a-star.edu.sg (L.P.S.); sre1@cam.ac.uk (S.R.E.)

Supplementary Materials for

Electrical Wind Force–Driven and Dislocation-Templated Amorphization in Phase-Change Nanowires

Sung-Wook Nam, Hee-Suk Chung, Yu Chieh Lo, Liang Qi, Ju Li, Ye Lu, A.T. Charlie Johnson, Yeonwoong Jung, Pavan Nukala, Ritesh Agarwal*

*To whom correspondence should be addressed. E-mail: riteshag@seas.upenn.edu

Published 22 June 2012, *Science* **336**, 1561 (2012)
DOI: 10.1126/science.1220119

This PDF file includes:

Other Supplementary Material for this manuscript includes the following:
(available at www.sciencemag.org/cgi/content/full/336/6088/1561/DC1)

Movies S1 to S3

Materials and Methods

1. Preparation of $Ge_2Sb_2Te_5$ nanowires

$Ge_2Sb_2Te_5$ (GST) nanowires were synthesized using the metal catalyst mediated vapor–liquid–solid (VLS) process (*3*,*8*). Bulk GeTe and Sb_2Te_3 powders (99.99%, Sigma-Aldrich) were separately located inside a horizontal tube furnace in different temperature zones. GeTe (T_m=724 ^oC) powder was placed in the middle of the furnace and Sb_2Te_3 (T_m=617 ^oC) at the upstream side (5 cm away from the middle of the furnace). The silicon substrate coated with sputtered-Au/Pd film was placed at the downstream side of the furnace (~20 cm away from the middle). The furnace was ramped to 670 ℃ with a flow of Ar gas (130 sccm) at 100 torr pressure and maintained for 1 hour. After the growth, the furnace was slowly cooled down to room temperature. The as-grown nanowires were characterized by scanning electron microscopy (SEM, FEI DB strata 235 FIB and JEOL 7500F) and transmission electron microscopy (TEM, JEOL 2010F, 200 kV) equipped with EDS (Energy Dispersive Spectroscopy).

2. Device fabrication for in situ TEM observation

Devices compatible with in situ TEM holder have been carefully fabricated by a well-designed series of photolithography and etching steps. The fabrication steps are illustrated in Fig. S2. The images of in situ TEM chips so prepared, and electron beam transparent devices are shown in Fig.S3. Sculpting of a notch on the nanowire devices has been performed through Focused Ion Beam milling.

3. In situ TEM electric biasing experiment set up

All in situ TEM work has been done on the JEOL 2010F (200KeV, 400nm beam diameter, ~10nA current), at the Penn Regional Nanotechnology Facility. The entire experimental set-up has been illustrated in Fig. S4.

4. DFT calculations

Ab initio total energy calculations based on density functional theory (DFT) were performed by using Vienna-ab-initio-simulation-package (VASP) (*23*,*24*). The ultra-soft (US) pseudopotentials (PP) with the projector augmented wave (PAW) method and the generalized-gradient approximations (GGA) were used. The arrangement of GST atomic stacking sequence was referred to a stable hexagonal crystal structure shown in Sun's works (*22*). Before estimating the generalized-stacking-fault (GSF) energy, the super cell structure was relaxed by conjugate gradient algorithm to obtain equilibrium lattice constants and bond lengths. The k-point grids of the Monkhorst-Pack mesh for the Brillouin zone integration was $5 \times 5 \times 5$. The energy cut-off for plane waves was 227.47 eV and the convergence criteria for the electronic and ionic relaxation was 1×10^{-6} eV and 10^{-5} eV, respectively. The lattice constants and bond lengths after relaxations agree with Sun's values, except the space between Te-Te layers (4.13 Å) were a little bit larger than that (3.51 Å) in Sun's works, which may result from the inaccurate description of van der Waal interactions by DFT methods.

To compute the GSF energy (*23*) on basal plane, we set up a slab model with five GST primitive cells along [0001] axis and shifted it on the Te-Te basal plane along $\langle 11\bar{2}0 \rangle$ direction (Fig. S11A and B). The k-point mesh of $5 \times 5 \times 1$ were automatically created with Gamma symmetry. For GSF on prismatic plane, we set up a slab model with five $\langle 11\bar{2}0 \rangle$ GST primitive cells along $\langle 2\bar{1}\bar{1}0 \rangle$ axis and slid half of the unit cell on the prismatic plane along direction (shown in Fig. S15C), and $5 \times 1 \times 5$ k-point on Monkhorst-Pack mesh was applied. In addition, the shear modulus was calculated by tilting the unit cell within a small angle ($< 1^o$) on both basal and prismatic planes with certain specific directions, as summarized in Fig. S15.

Supplementary Text

1. Characterization of resistance dip

Using nanowires of different diameters and electrical pulses of varying amplitudes and widths, critical voltages required for the initiation of the resistance dip have been identified. The data is presented in Fig. S5.

2. Characterization of dislocations

Dislocations have been characterized through the HRTEM images. Fig.S6. shows the possible Burgers vectors of prismatic loops generated during electrical programming

3. Characterization of the amorphized region and the dislocation cloud (From Fig. 2 and 3 of the main manuscript)

Dislocation cloud contrast has been characterized by Dark-field TEM imaging. The dislocation cloud templates the cross-section of the nanowire, amorphizing it along the template. Amorphous region has been confirmed via HRTEM analysis. The results are shown in Fig.S7 and Fig.S8.

4. Explanation of dislocation dynamics in $Ge_2Sb_2Te_5$ nanowires

Figures S11 to S14 illustratively explain the formation of prismatic loops (two kinds), and their glide planes, and the reason why these loops on an average move along the wind-force direction

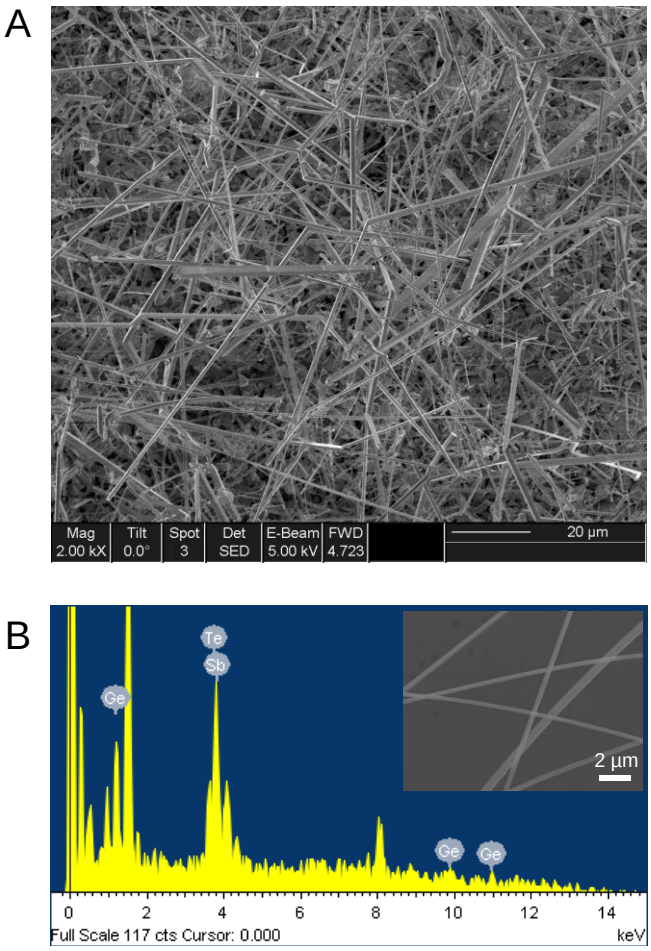

Fig. S1: (A) Scanning electron microscope (SEM) image of as-grown GST nanowires. (B) Energy dispersive spectroscopy (EDS) data of the GST single nanowire. (inset) SEM image of nanowires on a carbon-coated grid

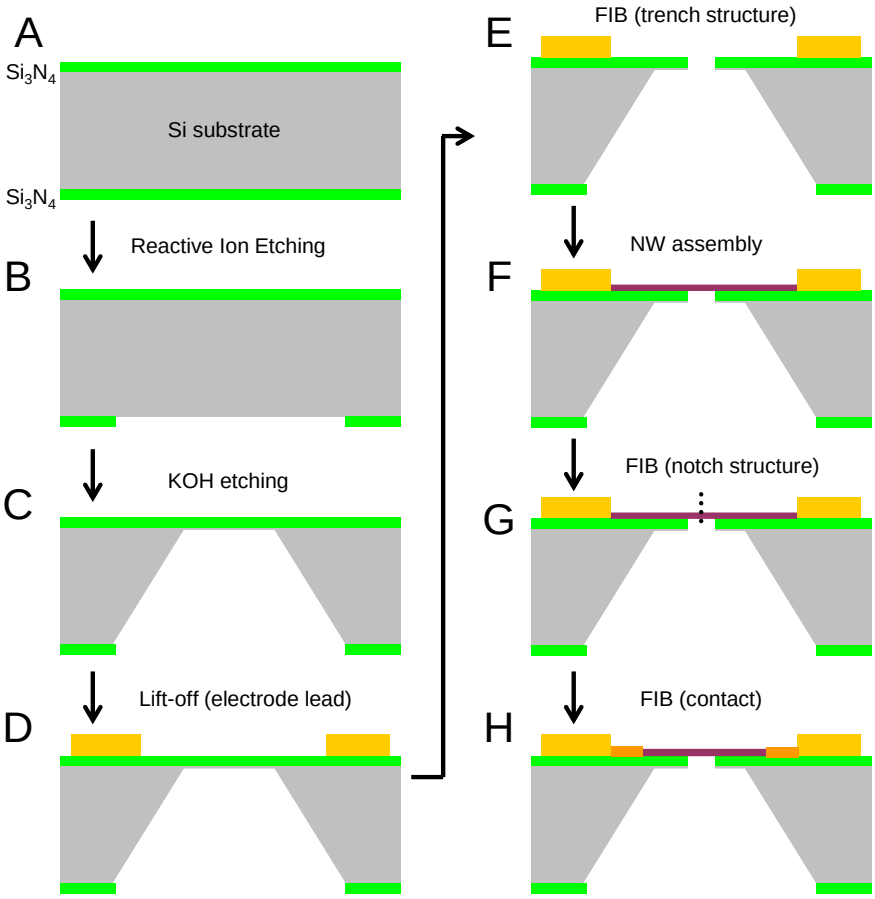

Fig. S2: Process sequence of the fabrication of nanowire devices for in situ TEM experiments: (A) Silicon-nitride film (300 nm thickness, LPCVD, low stress) was deposited on both sides of silicon substrate (~500 µm thickness). (B) On the back-side of the wafer, a square shape (940 µm ×940 µm) was patterned by photolithography and the back side silicon nitride was selectively removed by SF_6-based reactive ion etching (RIE). (C) Anisotropic etching of bulk silicon was carried out by KOH at ~80 ^oC for ~5 hours to fabricate the silicon nitride membrane structure. (D) On the front side of the membrane, electrode leads were patterned by lift-off process. During photolithography, the electrode patterns were carefully aligned with the membrane region. Ti (~5 nm)/Au (~50 nm) was deposited by e-beam evaporator, and the sample was dipped in acetone for ~10 hours for lift-off process followed by rinsing in isopropyl alcohol (IPA). (E) Trench structures (~1 µm width) were patterned by focused ion beam (FIB); (3000 pA Ga^+ ion beam). (F) Vapor-liquid-solid (VLS) grown GST nanowires were transferred on the membrane by gently rubbing the as-grown sample on the patterned membranes. (G) The nanowires crossing the trench were selected, followed by sculpting the notch structure (for notched devices) (*3,8*). (H) Pt-electrode contacts were formed by FIB. See Fig. S3 for images of the final device.

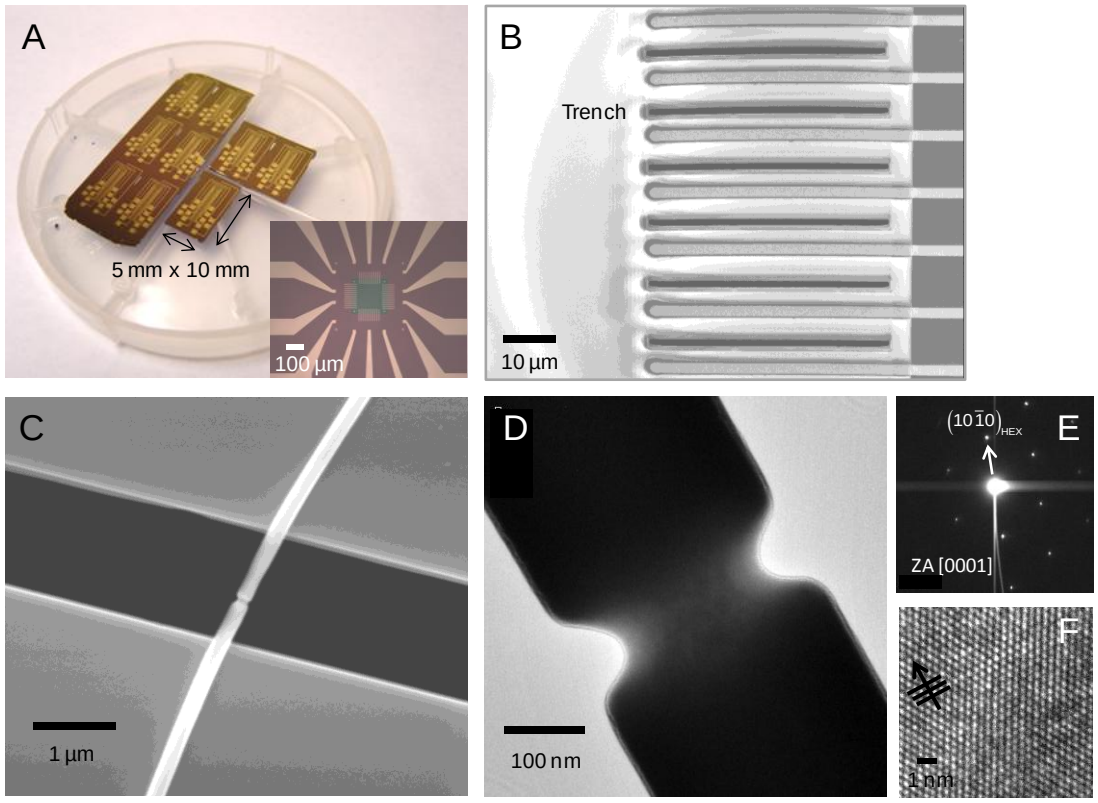

Fig. S3: Phase change GST nanowire devices: (A) Digital camera image and optical microscope image of the membrane device platform where the silicon nitride membrane was aligned with electrode leads. (B) SEM image of trench structures on silicon nitride membrane. (C) SEM image of free-standing nanowire crossing the trench region. (D) Dark field TEM image of the notched structure nanowire. (E, F) Diffraction pattern (of hexagonal crystal structure) and high-resolution TEM images of the nanowire: The dark arrow in F indicates the growth direction of the nanowire, perpendicular to the $(10\bar{1}0)$ prismatic plane.

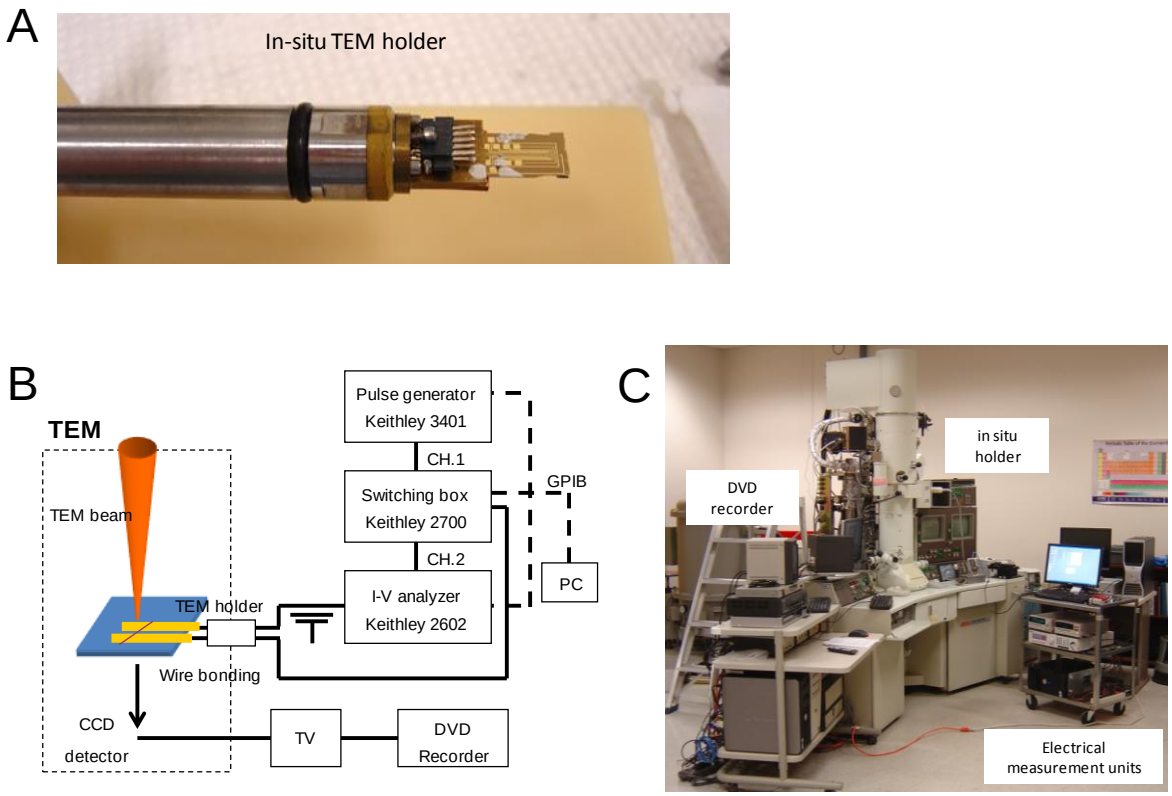

Fig. S4. (A) In situ TEM holder with electrical feed-throughs on which the nanowire devices on the membrane platform were mounted (*8*). Au-wire was connected between the device and the electrical line of the holder. (B) Schematic of the configuration for the electrical measurement units. All electrical measurements were performed with Keithley 2602 (I-V analyzer), Keithley 2700 (switching box), and Keithley 3401 (pulse-generator). (C) Jeol 2010F TEM where the in situ holder and the electrical measurement units are connected to enable in situ TEM measurements.

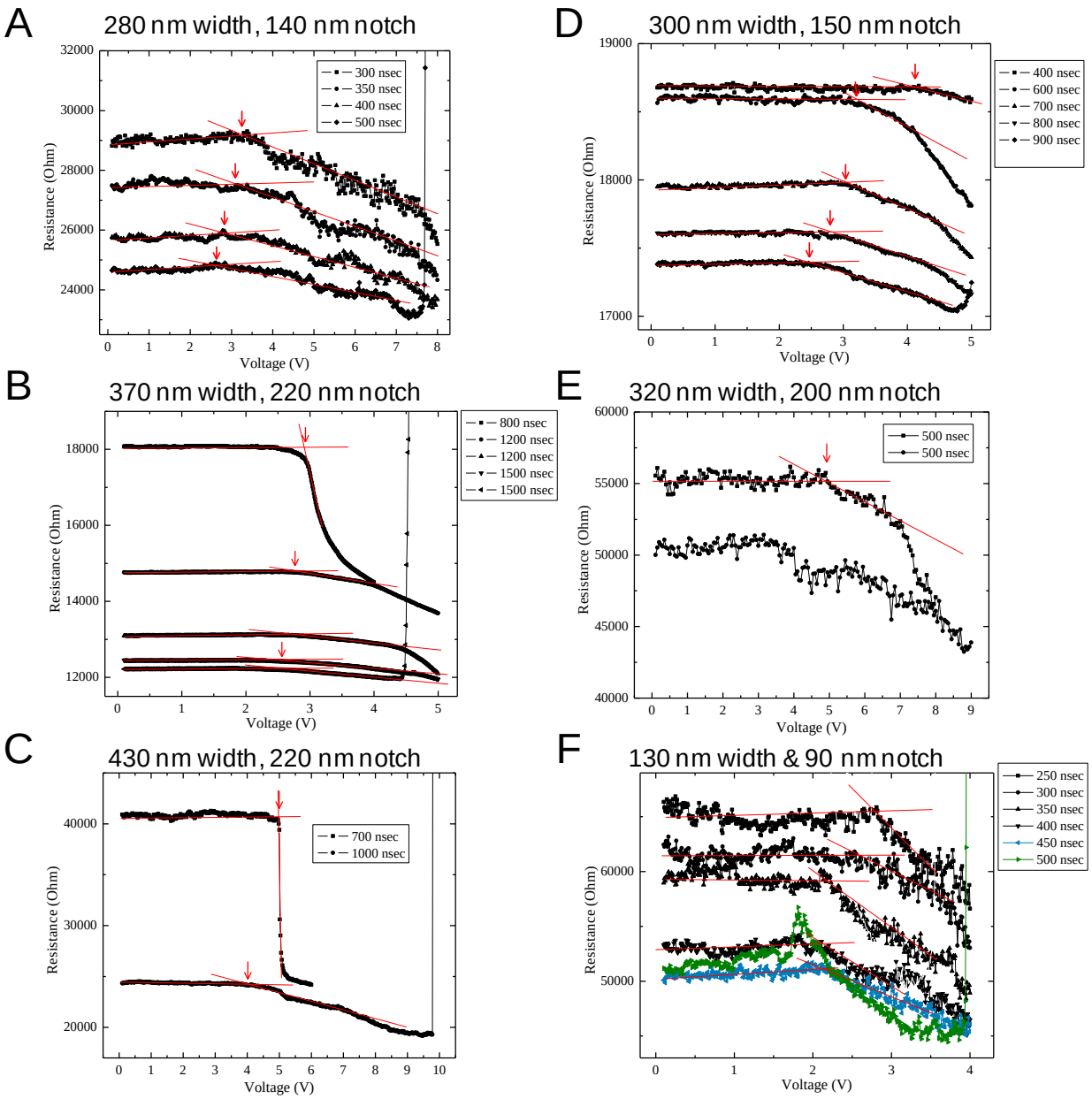

Fig S5 (A-F): Evaluation of the critical voltage amplitude (pulse) where the resistance dip was initiated

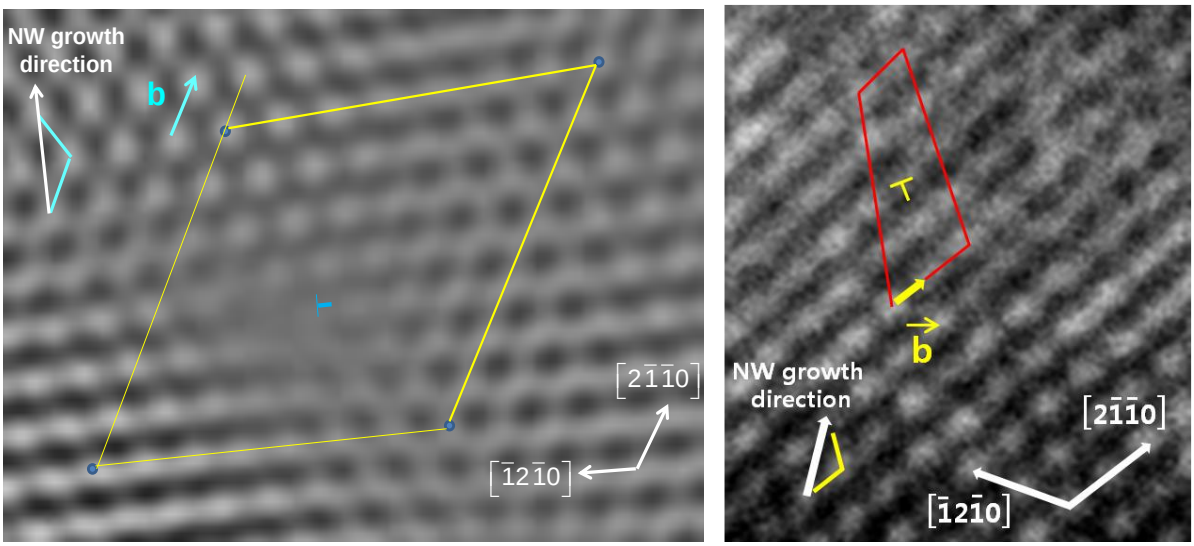

Fig S6:(Left) Burgers circuit of GST nanowire upon application of voltage pulses from Inverse Fast-Fourier Transformed High-resolution (HR) TEM image: The Burgers vector (*b*) was determined as $1/3\langle 11\bar{2}0\rangle$. (Right) High-resolution (HR) TEM image (no image processing) of dislocation in GST nanowire upon application of voltage pulses: The Burgers Circuit with extra half plane is shown.

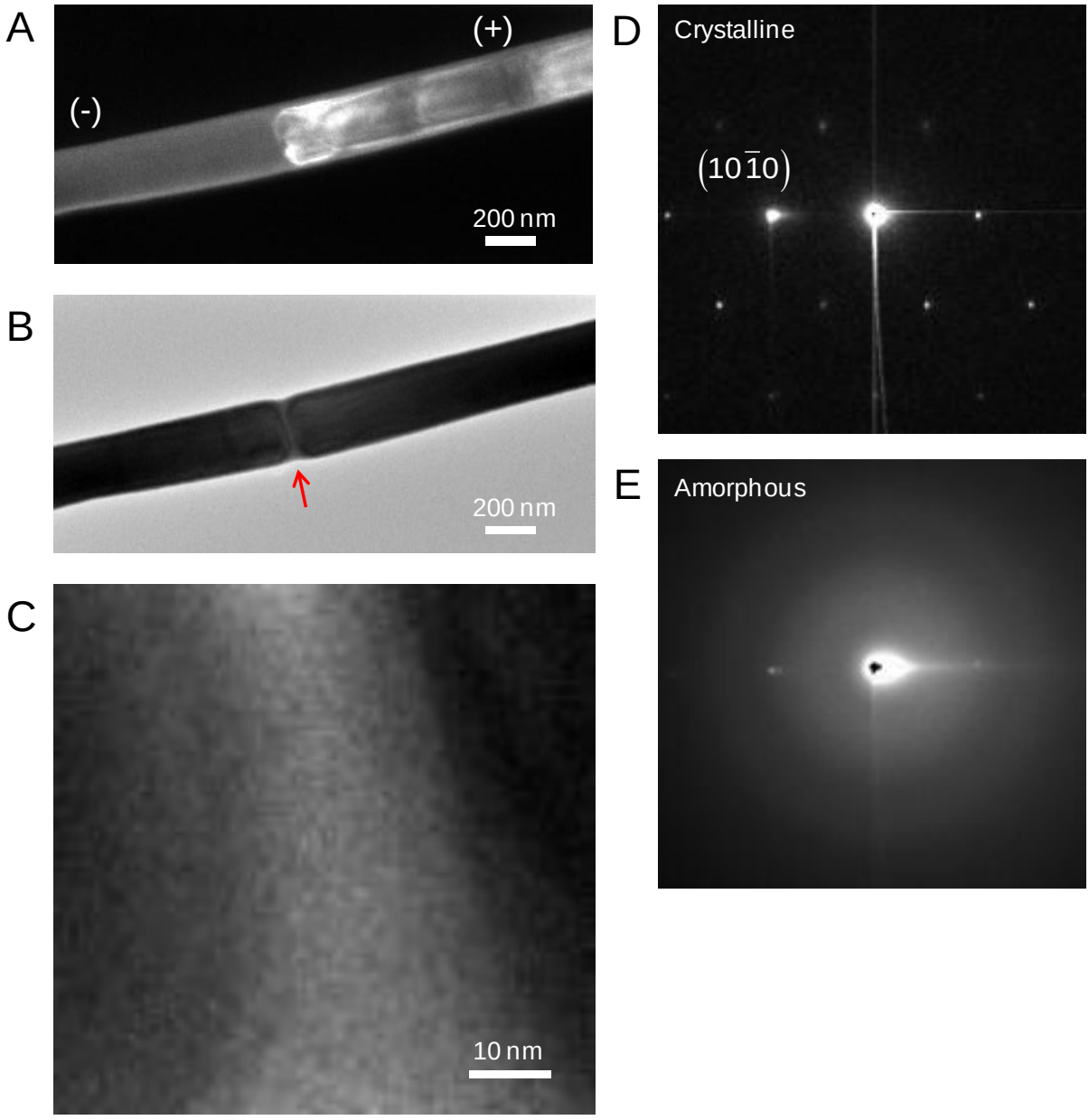

Fig. S7. TEM images of a non-notched nanowire device after amorphization switching. (A) A dark-Field (DF) image showing that the dislocation-cloud was developed at the (+) electrode region, behind the amorphized region. (B) A bright-field (BF) image where the amorphous structure was generated, as indicated by red-arrow. (C) Magnified image of the amorphous region which is sandwiched by crystalline regions. (D, E) Diffraction patterns obtained from the crystalline and the amorphous state regions, respectively.

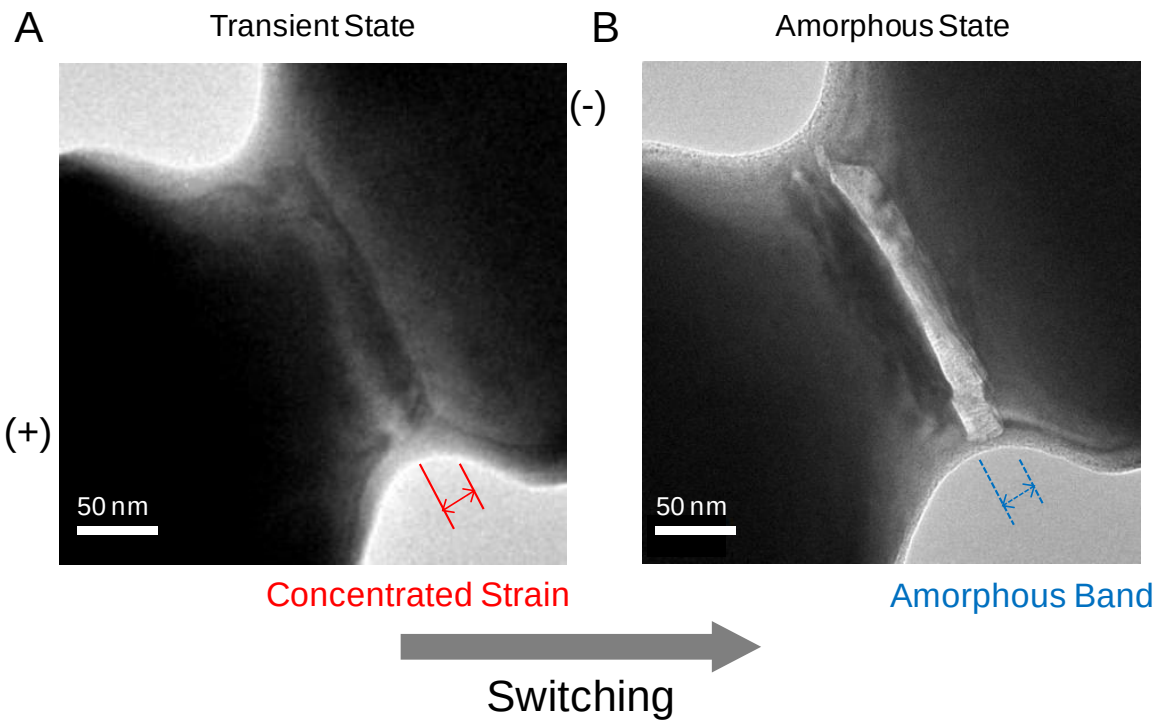

Fig. S8. Bright-field (BF) TEM images of a notched nanowire device (A) just before and (B) after amorphization switching. The highly concentrated strain (dark line in the middle of the notch) in (A) was switched into a bright-amorphous band in (B). The device is still crystalline in (A). The images are zoomed-in higher quality images from Fig. 3C and D from the main manuscript.

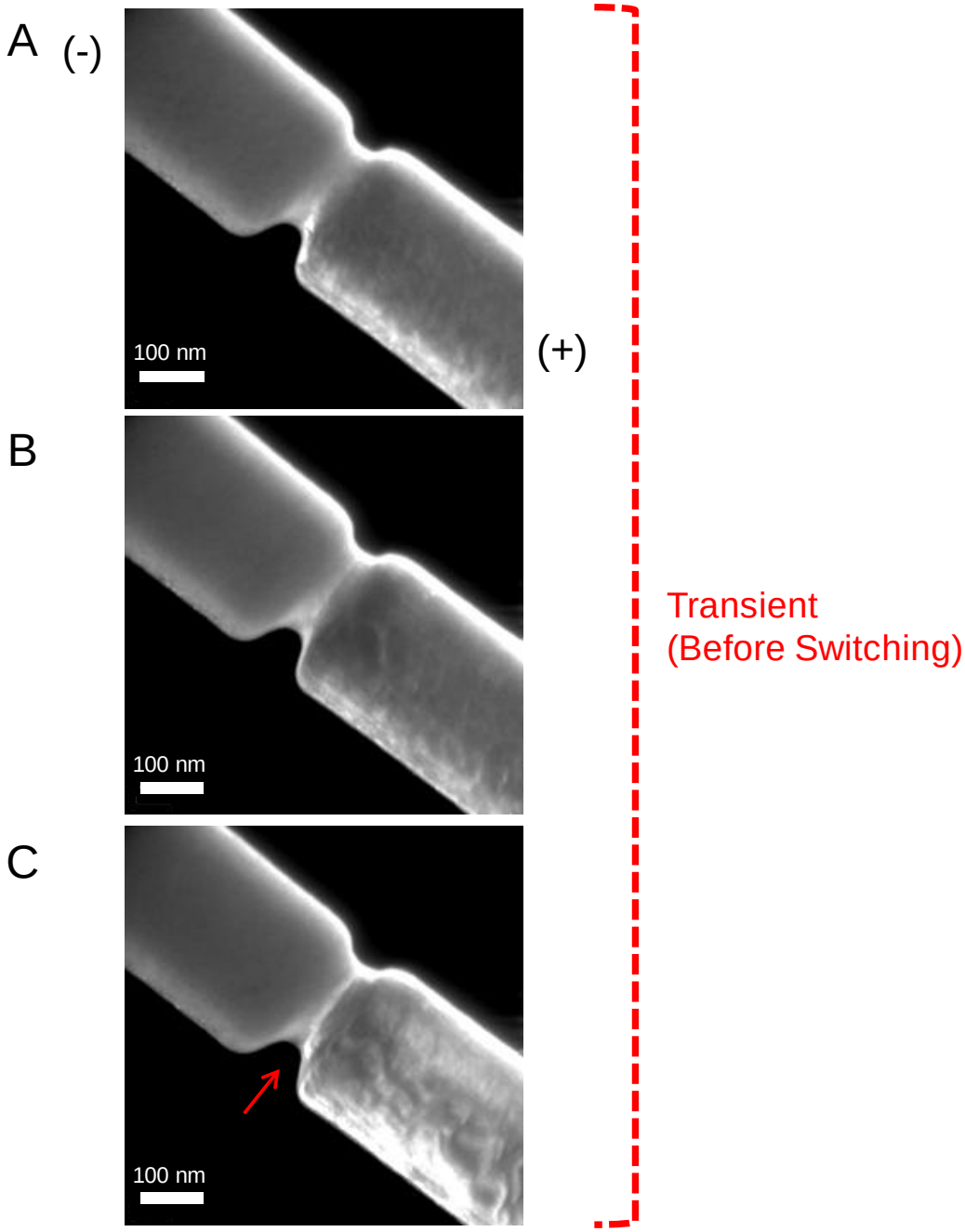

Fig S9: Dark-field (DF) TEM images of another notched nanowire device before amorphization switching: As the voltage pulse amplitude was increased from (A) to (C), the bright contrast from defect structures became more pronounced. The image contrast variations were observed predominantly at the (+) electrode region. The bright-band indicated by red-arrow in (C) corresponds to the highly-strained structure, as also described in Fig. S8A.

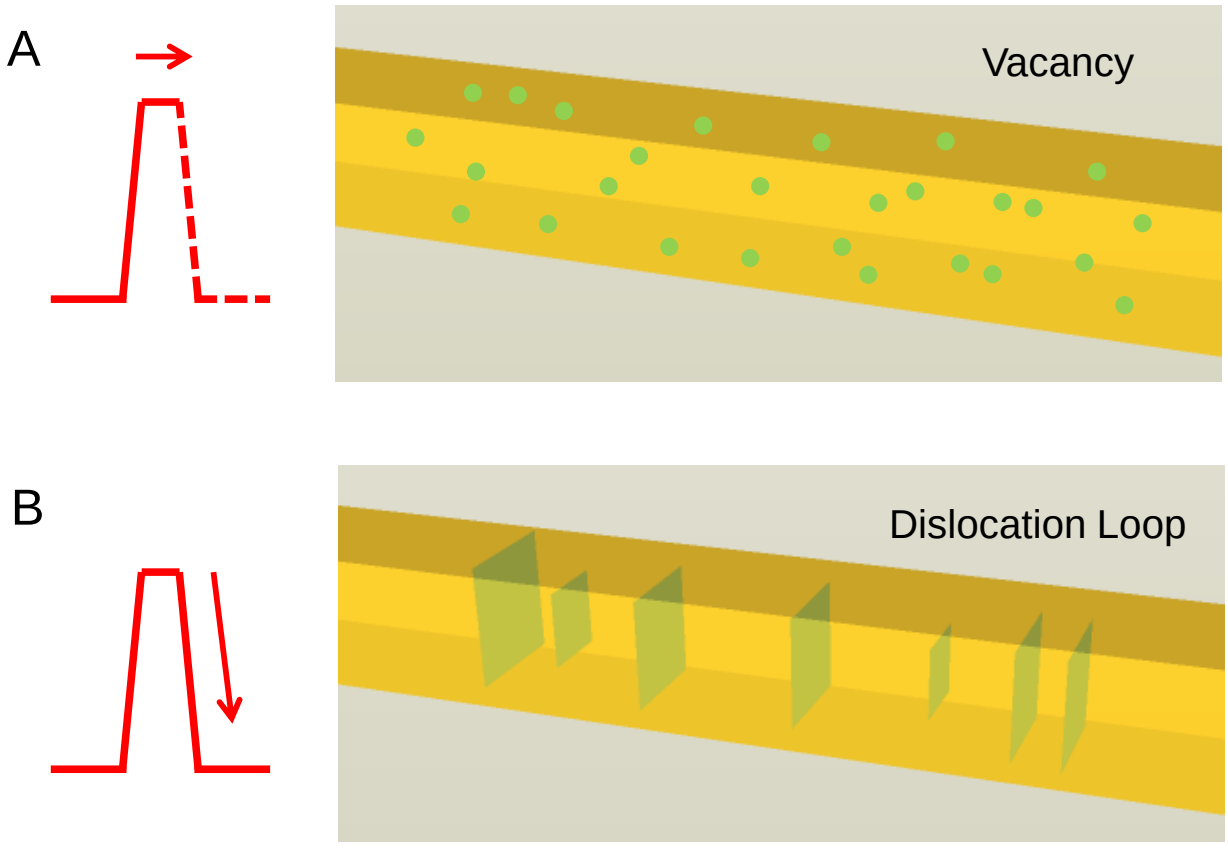

Fig. S10. Illustration of the heat-shock process that leads to the formation of dislocation loops in a GST nanowire during voltage pulsing: (A) During the rising edge of the electrical pulse, atomic vacancies are generated. (B) During rapid cooling (falling edge), dislocations loops are formed due to the condensation of the atomic vacancies.

$b_1 \equiv [11\underline{2}0]/3 = -a_3$; $b_2 \equiv [2\underline{11}0]/3 = a_1$; c=[0001]; $a_2 \equiv [\underline{1}2\underline{1}0]/3$

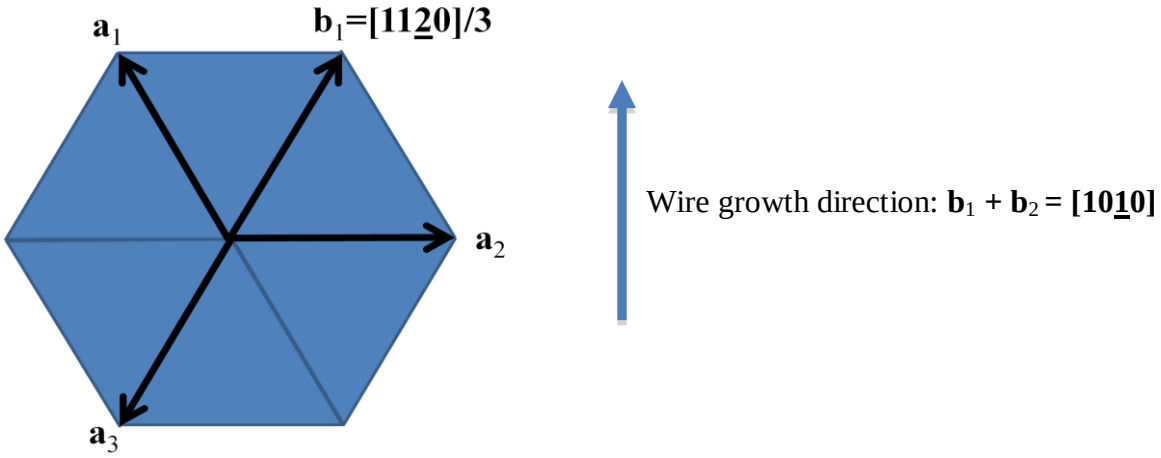

Fig S11: Illustration of the notation used in reference to the crystallographic directions for the GST nanowires used in our study.

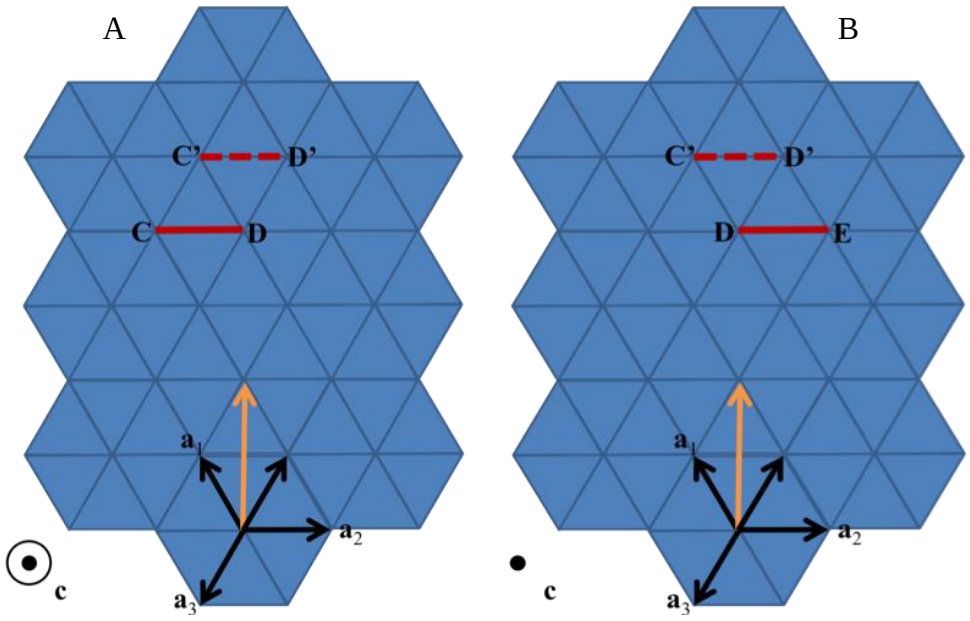

Fig S12: The crystallographic projection of the nanowire as seen inside the TEM. (A) A prismatic loop may be created by removing a plane of atoms C'D' and gluing CD onto where C'D' was. This process would create a dislocation loop with Burgers vector $\mathbf{b}_1$. (B) An energetically equivalent process is to remove the plane of atoms C'D', and glue DE to where C'D' was This process would create a dislocation loop with Burgers vector $\mathbf{b}_2$. These loops have 4 segments each, two in $\mathbf{a}_2$ direction, and two in **c** direction.

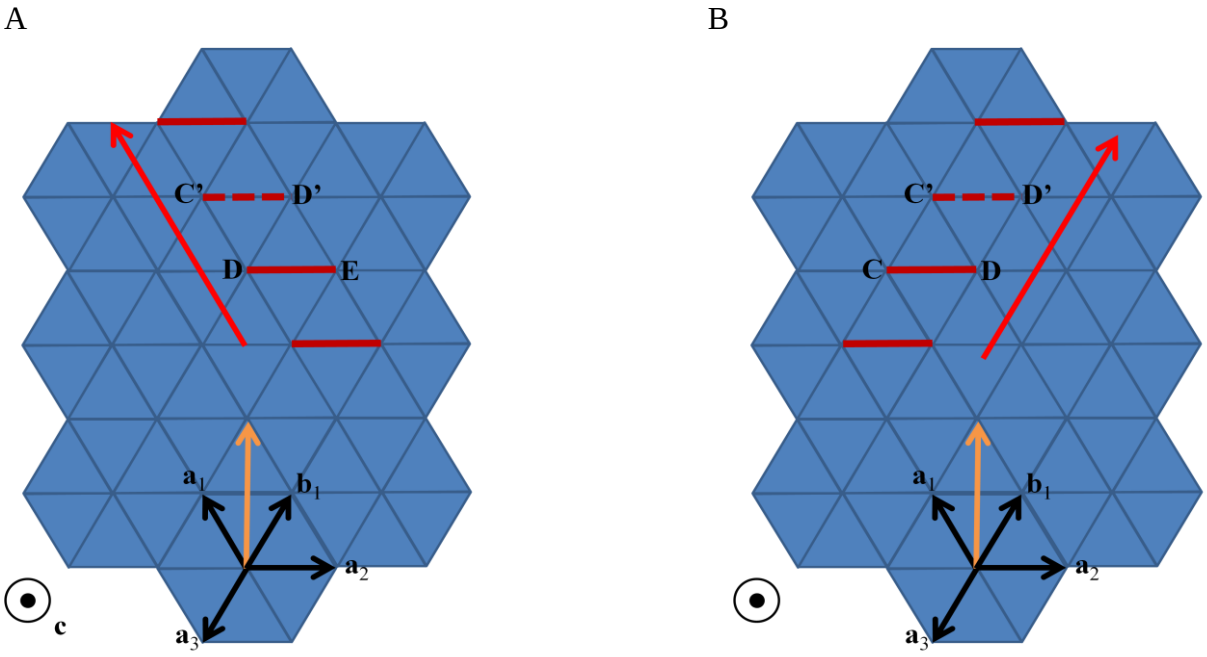

Fig S13: Illustration of two shear systems for the (A) $\mathbf{b_1}$ prismatic loop- (0001)[11$\underline{2}$0] and (1$\underline{1}$00)[11$\underline{2}$0], and (B) for $\mathbf{b_2}$ prismatic loop- (0001)[2$\underline{11}$0] and (1$\underline{1}$00)[2$\underline{11}$0]. Both these kinds of loops can glide as illustrated above like a domino cascade and eventually move out of the nanowire (cleaning up the garbage of vacancies along the way). Our computed GSF energy (pure displacive shear, no climb; figure 4 of the original manuscript) for (0001)[11$\underline{2}$0] and (1$\underline{1}$00)[11$\underline{2}$0] slip systems is 10.1 mJ/m^2 and 172.8 mJ/m^2 respectively which are quite low (GSF in Cu 169 mJ/m^2*(23)*).

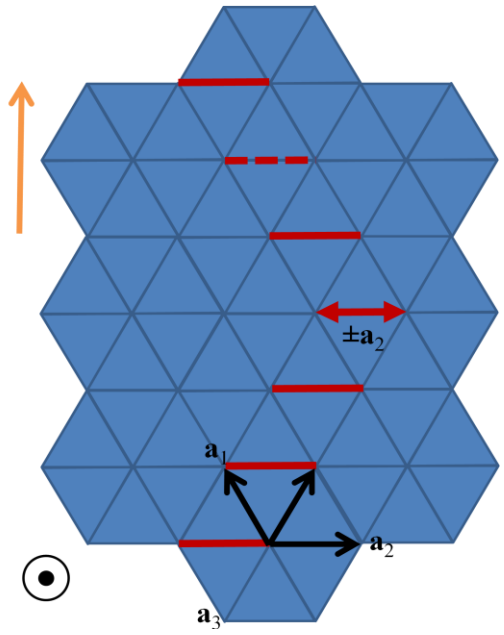

Fig S14: Illustration of gliding of dislocations in an average direction of the wind-force represented by the arrow in orange. $\mathbf{b_1}$ prismatic loops and $\mathbf{b_2}$ prismatic loops can toggle between each other by nucleating a shear loop with burgers vector $\mathbf{a_2}$, as shown above, which is not a difficult process (GSF energy for $(10\underline{1}0)[\underline{1}2\underline{1}0]$ slip system of 172.8 mJ/m^2)

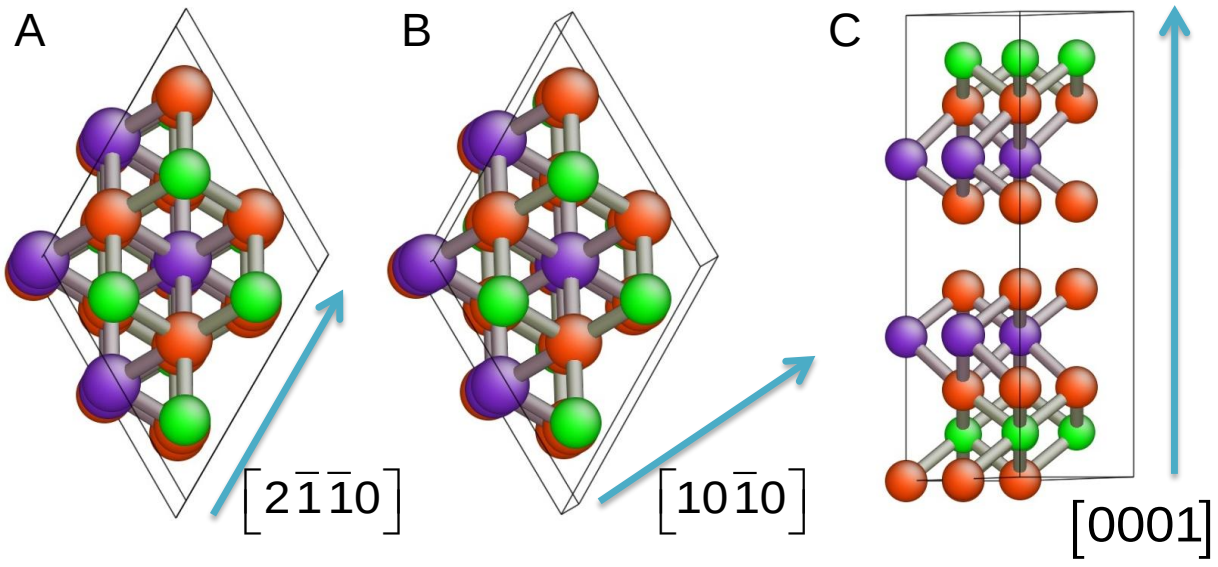

		G (GPa)	γ (mJ/m^2)
Basal Plane	[2-1-10] (a-axis direction)	5.1	10.1
Basal Plane	[10-10] (NW growth direction)	3.8	
Prismatic Plane	[0001] (c-axis direction)	7.7	172.18

Fig. S15. DFT calculations for shear stress (G) and generalized-stacking-fault (GSF) energy (γ) for different slip-characters in hexagonal $Ge_2Sb_2Te_5$.

(A) $1/3\langle 11\bar{2}0\rangle$ on basal plane, (B) $1/2\langle 10\bar{1}0\rangle$ on basal plane, and (C) [0001] on prismatic plane. (Red: Te atom, Green: Ge atom, Purple: Sb atom)

Supporting Online Movies

Movie S1: The movie shows dark-field (DF) TEM recording of a 230 nm thick $Ge_2Sb_2Te_5$ (GST) nanowire device during the "forward" biased electrical pulse sweeping. Although forward-bias on a symmetric device carries no meaning by itself, the term is used to distinguish the case where the same device is studied with the bias polarity reversed (as in Movie S2). The amplitude of the applied voltage pulse is shown on the movie frames and information about the pulse width is also provided. No structural changes were identified in the observed area until ~5 V pulses (800 ns), but concomitant with the onset of the resistance dip, the uniform contrast of the single-crystalline device started to change dynamically, with extended line-shaped defects and other strain-related contrasts appeared in the probed region. Upon further increasing the voltage pulse amplitude (800 ns duration), the resistance dip was directly associated with the line-defects becoming mobile and propagating along the direction of hole-carrier motion. In particular, dynamic contrast changes were identified moving unidirectionally into and out of the observed region. Upon approaching the bottom of the resistance dip, it was observed that the dislocations stopped moving (jamming), followed by highly accumulated and entangled dislocation formation at the jammed location. Finally, amorphization switching was observed, accompanied by an increase in the electrical resistance by approximately two orders of magnitude. The movie is played at 2X speed.

Movie S2: The movie shows DF TEM recording of the same device as in Movie S1 during the reverse-bias electrical pulse sweeping. This movie was recorded after the previous forward-biased device (Movie S1) was switched back to the low resistance state (crystalline state). This movie consists of five sequential movies of different voltage pulse sweeping processes. Upon applying 500 ns-width pulses, the resistance dip was observed, during which the jammed dislocation cloud from the previous measurement was relieved by moving in the opposite direction. Upon applying 800 ns pulses (sweep from 0 V), dynamic contrast changes were observed to move in the opposite direction, which corresponded to the direction of the–hole-carriers in this configuration. Eventually, amorphization switching occurred at ~5.2 V with the dislocation cloud appearing behind the amorphous mark, consistent with the forward-bias experiments. The movie was played at 4X.

Movie S3: The movie shows bright-field (BF) TEM recording of the notch-geometry GST nanowire device with applied voltage pulses. As-fabricated nanowire shows a uniform dark contrast due to its single-crystalline structure. As the applied pulse voltage amplitude was increased, dynamic changes in contrast was observed to move along the hole wind force direction. Just before the amorphization switching process, a darker line contrast (highly concentrated strain) was identified in the middle of the notch. Upon transformation to the amorphous phase, the darker line contrast was abruptly changed into the bright amorphous band.

References and Notes

1. M. Wuttig, N. Yamada, Phase-change materials for rewriteable data storage. *Nat. Mater.* **6**, 824 (2007). doi:10.1038/nmat2009 Medline

2. S. Raoux, Phase change materials. *Annu. Rev. Mater. Res.* **39**, 25 (2009). doi:10.1146/annurev-matsci-082908-145405

3. Y. Jung, S. W. Nam, R. Agarwal, High-resolution transmission electron microscopy study of electrically-driven reversible phase change in ge2sb2te5 nanowires. *Nano Lett.* **11**, 1364 (2011). doi:10.1021/nl104537c Medline

4. B. J. Kooi, W. M. G. Groot, J. T. M. De Hosson, In situ transmission electron microscopy study of the crystallization of $Ge_2Sb_2Te_5$. *J. Appl. Phys.* **95**, 924 (2004). doi:10.1063/1.1636259

5. P. Fons *et al*., *Phys. Rev. B* **82**, 041203(R) (2010).

6. A. V. Kolobov, M. Krbal, P. Fons, J. Tominaga, T. Uruga, Distortion-triggered loss of long-range order in solids with bonding energy hierarchy. *Nat. Chem.* **3**, 311 (2011). doi:10.1038/nchem.1007 Medline

7. D. R. Strachan *et al*., Real-time TEM imaging of the formation of crystalline nanoscale gaps. *Phys. Rev. Lett.* **100**, 056805 (2008). doi:10.1103/PhysRevLett.100.056805 Medline

8. S. H. Lee, Y. Jung, R. Agarwal, Highly scalable non-volatile and ultra-low-power phase-change nanowire memory. *Nat. Nanotechnol.* **2**, 626 (2007). doi:10.1038/nnano.2007.291 Medline

9. S. W. Nam *et al*., Electric-field-induced mass movement of $Ge_2Sb_2Te_5$ in Bottleneck Geometry Line Structures. *Electrochem. Solid-State Lett.* **12**, H155 (2009). doi:10.1149/1.3079480

10. T. Y. Yang, I. M. Park, B. J. Kim, Y. C. Joo, Atomic migration in molten and crystalline $Ge_2Sb_2Te_5$ under high electric field. *Appl. Phys. Lett.* **95**, 032104 (2009). doi:10.1063/1.3184584

11. M. H. Lee *et al*., *IEEE International Electron Devices Meeting (IEDM)*, 28.6.1. (2010).

12. G. Schoeck, W. A. Tiller, On dislocation formation by vacancy condensation. *Philos. Mag.* **5**, 43 (1960). doi:10.1080/14786436008241199

13. H. Kimura, R. Maddin, D. Kuhlmannwilsdorf, Quenched-in vacancies in noble metals—I theory of decay. *Acta Metall.* **7**, 145 (1959). doi:10.1016/0001-6160(59)90067-7

14. H. Zheng *et al*., *Nat. Commun.* **1**, 144 (2010).

15. Z. W. Shan, R. K. Mishra, S. A. Syed Asif, O. L. Warren, A. M. Minor, Mechanical annealing and source-limited deformation in submicrometre-diameter Ni crystals. *Nat. Mater.* **7**, 115 (2008). doi:10.1038/nmat2085 Medline

16. S. H. Oh, M. Legros, D. Kiener, G. Dehm, In situ observation of dislocation nucleation and escape in a submicrometre aluminium single crystal. *Nat. Mater.* **8**, 95 (2009). doi:10.1038/nmat2370 Medline

17. Q. Yu *et al*., Strong crystal size effect on deformation twinning. *Nature* **463**, 335 (2010). doi:10.1038/nature08692 Medline

18. T. Zhu, J. Li, A. Samanta, A. Leach, K. Gall, Temperature and strain-rate dependence of surface dislocation nucleation. *Phys. Rev. Lett.* **100**, 025502 (2008). doi:10.1103/PhysRevLett.100.025502 Medline

19. M. Mitra, Y. Jung, D. S. Gianola, R. Agarwal, Extremely low drift of resistance and threshold voltage in amorphous phase change nanowire devices. *Appl. Phys. Lett.* **96**, 222111 (2010). doi:10.1063/1.3447941

20. R. H. Telling, M. I. Heggie, Stacking fault and dislocation glide on the basal plane of graphite. *Philos. Mag. Lett.* **83**, 411 (2003). doi:10.1080/0950083031000137839

21. A. V. Kolobov *et al*., Understanding the phase-change mechanism of rewritable optical media. *Nat. Mater.* **3**, 703 (2004). doi:10.1038/nmat1215 Medline

22. Z. M. Sun, J. Zhou, R. Ahuja, Structure of phase change materials for data storage. *Phys. Rev. Lett.* **96**, 055507 (2006). doi:10.1103/PhysRevLett.96.055507 Medline

23. S. Ogata, J. Li, S. Yip, Energy landscape of deformation twinning in bcc and fcc metals. *Phys. Rev. B* **71**, 224102 (2005). doi:10.1103/PhysRevB.71.224102

24. E. Kaxiras, M. S. Duesbery, Free energies of generalized stacking faults in Si and implications for the brittle-ductile transition. *Phys. Rev. Lett.* **70**, 3752 (1993). doi:10.1103/PhysRevLett.70.3752 Medline

25. D. Hull, D. J. Bacon, *Introduction to Dislocations* (Butterworth-Heinemann, Oxford, ed. 4, 2001).

26. K. Nagel, Particle hopping models and traffic flow theory. *Phys. Rev. E Stat. Phys. Plasmas Fluids Relat. Interdiscip. Topics* **53**, 4655 (1996). doi:10.1103/PhysRevE.53.4655 Medline

27. D. Helbing, Traffic and related self-driven many-particle systems. *Rev. Mod. Phys.* **73**, 1067 (2001). doi:10.1103/RevModPhys.73.1067

28. D. Wolf, P. R. Okamoto, S. Yip, J. F. Lutsko, M. Kluge, Thermodynamic parallels between solid-state amorphization and melting. *J. Mater. Res.* **5**, 286 (1990). doi:10.1557/JMR.1990.0286

29. J. Y. Huang, H. Yasuda, H. Mori, Deformation-induced amorphization in ball-milled silicon. *Philos. Mag. Lett.* **79**, 305 (1999). doi:10.1080/095008399177147

30. J. Y. Huang *et al*., In situ observation of the electrochemical lithiation of a single SnO_2 nanowire electrode. *Science* **330**, 1515 (2010). doi:10.1126/science.1195628 Medline

31. J. Y. Huang, Y. T. Zhu, X. Z. Liao, R. Z. Valiev, Amorphization of TiNi induced by high-pressure torsion. *Philos. Mag. Lett.* **84**, 183 (2004). doi:10.1080/09500830310001657353

32. Y. Mishin, M. Asta, J. Li, Atomistic modeling of interfaces and their impact on microstructure and properties. *Acta Mater.* **58**, 1117 (2010). doi:10.1016/j.actamat.2009.10.049

33. A. V. Kolobov *et al*., Pressure-induced site-selective disordering of $Ge_2Sb_2Te_5$: A new insight into phase-change optical recording. *Phys. Rev. Lett.* **97**, 035701 (2006). doi:10.1103/PhysRevLett.97.035701 Medline

MATERIALS SCIENCE

Primed to Remember

With the potential to mimic the human brain, phase-change memories are operating faster, while imaging provides further insight into the switching mechanism.

Dan Hewak and Behrad Gholipour

Human memory can be primed. Expose the brain, even unconsciously, to a word or object, and in subsequent exposures, the memory synapses are faster, and more details are remembered for longer times (*1*). Why not do the same with the electronic memories in our computers, phones, digital cameras, and game consoles? On page 1566 of this issue, Loke *et al*. (*2*) show that writing speeds in next-generation electronic memory—ones based on changing a material's phase from a crystal to a glass—have increased substantially through a preswitching incubation process. This priming enabled them to break the 1-ns barrier for electronic switching. On page 1561, Nam *et al*. (*3*) remarkably provide images and recordings of the electronic changes that occur in memory cells only a few nanometers in size that allow us to watch the switching mechanism. Both of these studies provide valuable information on the physics of phase-change memory (PCM) and also clues on how this technology could change computer architectures.

The most common nonvolatile memory (one that retains data with the power off) used in laptop computers, smartphones, and video-game consoles is flash memory, which traps a few electrons within an electronic "gate"; the charged state represents a bit of information. However, the size of flash memory cells has been shrunk to near fundamental limits; smaller cells would lose memory information from electrons leaking through the gate into neighboring cells.

Unlike flash memory, PCM does not depend on trapped electrons, and memory cells can be reduced to much smaller sizes. Phase-change materials for memory applications are typically metallic alloys, commonly based on germanium, antimony, and tellurium ($Ge_2Sb_2Te_5$, or GST). These compounds can easily be switched between the amorphous and crystalline phase, by heating with a laser (as in a DVD or CD disk), or with a small electrical current when the GST is part of an electronic memory chip. Like flash memory, PCM is nonvolatile, and once switched, the phase remains stable until the cell is rewritten. In addition to smaller cell sizes, PCM is inherently faster and can switch repeatedly tens of millions of times, versus only several thousand times for flash memory. Electronic PCM could allow computers to boot instantaneously and greatly enhance the overall performance of computer networks. Many researchers argue that these materials will provide a universal memory technology that could replace both magnetic hard drive and dynamic random-access memory, and even mimic the human brain (*4*).

Breaking the speed limits of PCM is how Loke *et al*. describe their recent advances. Priming of human memory works best when the two stimuli are in the same modality (e.g., visual priming works best with visual cues). A weak electric current primed the cell, then a short higher-intensity pulse stored the bit of information. This tandem process significantly sped up crystallization;

Optoelectronics Research Centre, University of Southampton, Southampton SO17 1BJ, UK. E-mail: dh@orc.soton.ac.uk; bg305@orc.soton.ac.uk

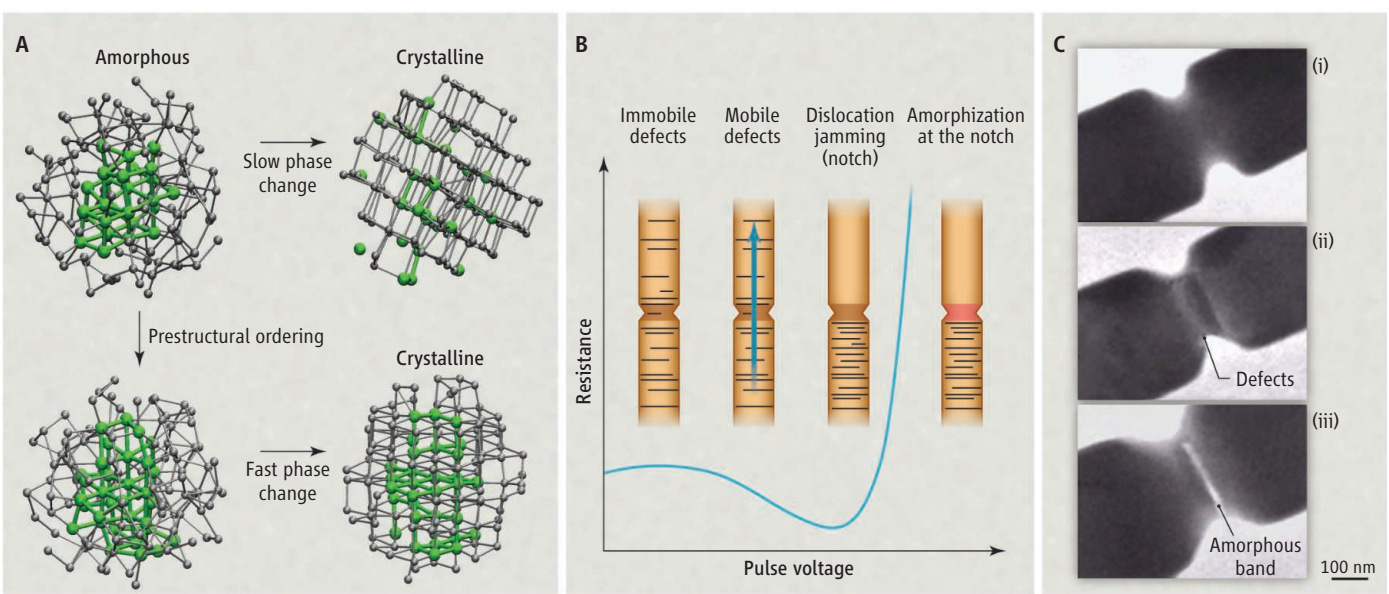

Making memories. (**A**) Model configurations generated by Loke *et al*. of atomic rearrangements during phase transition with or without prestructural orders (priming) that sped up the phase change. (**B**) This schematic shows dislocation nucleation, transport, and jamming by electrical pulses observed by Nam *et al*., along with corresponding changes in electrical resistance. Electrical pulses induce heat shocks that nucleate dislocations from atomic vacancies. Larger pulse voltages caused the dislocations to move along the direction of holes. At high dislocation densities, a jamming transition (e.g., in the notch region or elsewhere for regular wires) occurred as dislocations piled up, and the resistance minimized. Further pulses created an amorphous region and a more insulating phase. (**C**) A series of snapshots from a bright-field TEM movie by Nam *et al*. in which the as-fabricated nanowire initially shows a uniform dark contrast along the nanowire (i). As electrical pulses were applied, a variation in contrast was seen, with the darker line in the middle of the notch (ii) indicating a region of high strain. This region changed into bright contrast upon amorphization (iii).

Published by AAAS

switching speeds of 500 ps were reached for the smallest cells. They used computer simulations to help identify a structural origin to this speed increase, which they believe is induced through thermal prestructuring (see the figure, panel A). As measured during this electronic priming, a resistance dip suggests some permanent preswitching structural modification.

The effects of priming the human brain can be imaged by monitoring the brain's frontal region activity using an electroencephalogram (*5*). In an analogous fashion, Nam *et al*. extend our understanding of the phase-change mechanism by using in situ transmission electron microscopy (TEM) to watch switching directly. By using single-crystal GST nanowires, which provide an open geometry, they viewed the material during the actual switching process (see the figure, panel B). Their direct observation of amorphization in a crystalline phase-change material revealed astonishing insight into the phase-change mechanism. When a voltage was applied across the nanowire, the TEM imaging showed visible contrast changes associated with the now characteristic resistance dip. With a continuously increasing current, defects became mobile and began to propagate along the direction of hole-carrier motion.

At the point of lowest resistance, the movement jammed and a tangled region of highly accumulated dislocations formed, which was followed by switching into an amorphous state. This glassy state appeared as a clear bright line and was confirmed as amorphous by electron diffraction measurements. Nam *et al*. make the analogy of traffic on a highway, in which a simple analytical model predicts a sharp catastrophic jamming transition when the vehicle density exceeds a certain fraction of the maximum packing density (*6*). In an inspired next step, they created a notch in their nanowire, akin to closing a lane on a busy highway. Defects piled up and an amorphous band appeared at the restriction (see the figure, panel C).

Recently, it has been argued that PCM materials do not change from glass to crystal by melting to a liquid and resolidifying, but rather transform via an all solid-state process. Nam *et al*. may have provided visual evidence of this hypothesis. As Kolobov *et al*. (*7*) explained, "distortions in the crystalline phase may trigger a collapse of long-range order, generating the amorphous phase without going through the liquid state, upsetting yet another commonly held belief that attributes the change in properties to the loss of long-range order."

Unlike human brains, today's computers deal with processing and memory separately. Data are constantly moved around, resulting in a speed and power "bottleneck." Kuzum *et al*. (*8*) describe brain-inspired computing and identified phase-change materials as ideal for the implementation of synaptic plasticity. Unlike binary memory applications, they used the continuous transition between resistance levels of phase-change states in an analog manner to emulate biological synapses. Wright *et al*. demonstrated that phase-change materials can both store and process information simultaneously (*9*) and could be used to make artificial neurons and synapses. Another major hurdle is power consumption; supercomputers consume substantially more energy than the human brain while "thinking" (*10*). These studies, along with recent new PCM designs by Xiong *et al*. (*11*), show that there is promise for power reductions through the use of PCM technology.

The studies by Loke *et al*. and Nam *et al*., along with related work in other labs, should not only pave the way for phase-change memories with ultrafast switching speeds, low-energy consumption, and reduced memory cell sizes, but also lead to a better understanding of the mechanisms responsible for the phase-change phenomena that could further improve switching speeds. The potential to emulate the human nervous system is gaining increasing attention, as these combined works provide further evidence that phase-change materials could be used to make artificial neurons and synapses.

References

1. E. Tulving, D. L. Schacter, *Science* **247**, 301 (1990).
2. D. Loke *et al*., *Science* **336**, 1566 (2012).
3. S.-W. Nam *et al*, *Science* **336**, 1561 (2012).
4. D. Lencer, M. Salinga, M. Wuttig, *Adv. Mater. (Deerfield Beach Fla.)* **23**, 2030 (2011).
5. L. J. Otten, A. H. Quayle, S. Akram, T. A. Ditewig, M. D. Rugg, *Nat. Neurosci.* **9**, 489 (2006).
6. J. A. Dantzig, C. L. Tucker, *Modeling in Materials Processing* (Cambridge Univ. Press, Cambridge, UK, 2001).
7. A. V. Kolobov, M. Krbal, P. Fons, J. Tominaga, T. Uruga, *Nat. Chem.* **3**, 311 (2011).
8. D. Kuzum, R. G. D. Jeyasingh, B. Lee, H.-S. P. Wong, *Nano Lett.* **12**, 2179 (2012).
9. C. D. Wright, Y. Liu, K. Kohary, M. M. Aziz, R. J. Hicken, *Adv. Mater. (Deerfield Beach Fla.)* **23**, 3408 (2011).
10. M. Salinga, M. Wuttig, *Science* **332**, 543 (2011).
11. F. Xiong, A. D. Liao, D. Estrada, E. Pop, *Science* **332**, 568 (2011).

10.1126/science.1223365

ECOLOGY

Biotic Multipliers of Climate Change

Phoebe L. Zarnetske,[1] David K. Skelly,[1] Mark C. Urban[2]

A focus on species interactions may improve predictions of the effects of climate change on ecosystems.

Many species face uncertain fates under climate change. Some will persist by shifting their range or adapting to local conditions, whereas others will be lost to extinction. Efforts to lessen the impacts of climate change on biodiversity depend on accurate forecasts. Most studies aiming to identify likely winners and losers consider species one at a time with a "climate envelope" approach that correlates species' occurrences with climatic and environmental variables. Using this method, researchers have predicted that by 2050, 15 to 37% of species will be faced with extinction (*1*). But which species are most likely to be under threat? And how will their loss affect the broader ecological community?

The climate envelope approach ignores a core truth of ecology: Species interact with each other in ways that deeply affect their viability. Certain species impart particularly strong effects on others. Consequently, climate change impacts on these species could initiate cascading effects on other species. In effect, these species act as biotic multipliers of climate change. The inherent complexity of species interaction networks has discouraged their consideration in predictions. Emerging research illustrates that trophic interactors are especially strong candidates for biotic multipliers of climatic change. Focusing on these species and their interactions is one path through the complexity.

Recent findings highlight the importance of undisturbed vertical interactions involv-

[1]School of Forestry and Environmental Studies, Yale University, 195 Prospect Street, New Haven, CT 06511, USA. [2]Department of Ecology and Evolutionary Biology, University of Connecticut, 75 North Eagleville Road, Unit 3043, Storrs, CT 06269, USA. E-mail: phoebe.zarnetske@yale.edu